JGR Planets

RESEARCH ARTICLE
10.1029/2024JE008765

Describing the Global Gravity Field of Mars With Lithospheric Flexure and Deep Mantle Flow

Bart Root[1], Weilun Qin[1,2], Youandi van der Tang[1], and Cedric Thieulot[3]

[1]Department of Space Engineering, Delft University of Technology, Delft, The Netherlands, [2]Department of Geoscience & Remote Sensing, Delft University of Technology, Delft, The Netherlands, [3]Department of Earth Sciences, Utrecht University, Utrecht, The Netherlands

Key Points:

- Global flexural model of the Martian lithosphere and crustal structure based on gravity observations
- Evidence of a deep mantle anomaly with positive buoyancy underneath the Tharsis Region
- Subsurface high mass anomalies in the northern polar crust showing no topographic expression

Supporting Information:

Supporting Information may be found in the online version of this article.

Correspondence to:

B. Root,
b.c.root@tudelft.nl

Citation:

Root, B., Qin, W., van der Tang, Y., & Thieulot, C. (2026). Describing the global gravity field of Mars with lithospheric flexure and deep mantle flow. *Journal of Geophysical Research: Planets*, *131*, e2024JE008765. https://doi.org/10.1029/2024JE008765

Received 5 OCT 2024
Accepted 8 FEB 2026

Author Contributions:

Conceptualization: Bart Root, Cedric Thieulot
Formal analysis: Bart Root, Weilun Qin, Youandi van der Tang
Investigation: Bart Root, Youandi van der Tang
Methodology: Bart Root, Weilun Qin
Project administration: Bart Root
Resources: Bart Root
Software: Bart Root, Weilun Qin, Youandi van der Tang, Cedric Thieulot
Supervision: Bart Root
Validation: Bart Root, Cedric Thieulot
Visualization: Bart Root, Cedric Thieulot
Writing – original draft: Bart Root, Weilun Qin
Writing – review & editing: Bart Root, Weilun Qin, Youandi van der Tang, Cedric Thieulot

Abstract The volcanic complex Tharsis Region on Mars is known for its numerous volcanoes on top of the crust, elevated topography (doming), and a long-wavelength gravity anomaly correlated with the region. Flexural modeling of the lithosphere has commonly been used to understand the relationship between observed topography, crustal structure, and gravity, but no conclusive answers have been obtained due to the ambiguity of these models. NASA's InSight mission has brought new information about the Martian lithosphere, which warrants a reanalysis of the support of the Tharsis Region. After analyzing the topography and gravity data, we found that a thin shell model of Mars matches both the observed gravity field for spherical harmonic degrees higher than 8 and the crustal thickness at Elysium determined by the InSight mission. Our thin shell flexure model uses an average crustal thickness of 55 km, crustal density of 3,050 kg/m^3, average mantle density of 3,750 kg/m^3, and an elastic thickness (T_e) of 100 km. The mismatch between modeled and observed gravity field for the long-wavelengths (between $n = 2 - 8$ degrees) correlates with the Tharsis Region, suggesting active large-scale dynamic support of the volcanic region. After modeling this dynamic support, we concluded that a substantial negative mass anomaly (hot buoyant mantle material, or depleted mantle region) in the mid mantle underneath the Tharsis Rise can explain the long-wavelength gravity residual. The remaining short-scale gravity residual gives insight to the Martian crustal density distribution and seems to correlate with geological structures of Mars. Buried mass anomalies in the subsurface of the northern polar plains seem not to be related to any geological or surface expressions, suggesting a more complex geology of the northern Martian crust than is suggested by the surface topography.

Plain Language Summary The NASA InSight mission has given us new information about the crust of Mars, which means that we can reexamine how we understand the support for the Tharsis Rise. The gravity signal of its surface fits well with our model that represents the planet as a thin elastic shell. This model suggests that Mars can be modeled with a crust of about 55 km thick and elastic rigidity layer of approximately 100 km thick. However, even with this thin shell lithosphere model, there is still a difference between the predictions and what is observed in the gravity field around the Tharsis Region. We found that a large mass anomaly below Tharsis that moves upward inside the mantle (the layer beneath the crust) can explain the broad gravity field residuals. Moreover, we found hidden structures in the Martian crust that do not have surface expressions and that suggests a much more complex geology of Mars hidden by the surface.

1. Introduction

The Tharsis volcanic province on Mars is distinguished by its concentration of large volcanic edifices, broad dome-like topography (Neumann et al., 2001), and an associated long-wavelength gravity anomaly (Konopliv et al., 2016). Flexural modeling of the lithosphere has been widely employed to investigate the relationship among surface topography, crustal structure, and gravity in this region. However, interpretations remain inconclusive due to the non-uniqueness of model solutions and uncertainties in lithospheric properties. Recent constraints on the thermal and mechanical structure of the Martian lithosphere provided by NASA's InSight mission motivate a re-evaluation of the lithospheric support mechanisms responsible for the Tharsis rise (Banerdt et al., 2020). This volcanic complex contains some of the largest volcanoes in our Solar System, of which Olympus Mons (21.2 km height) is the highest of all. The construction of the Tharsis region is found to have started in the late Noachian (3.7 Ga) until the Amazonian (3.0 Ga) (Anderson et al., 2001), with activity declining over time. This was corroborated by later studies (Bouley et al., 2018; J. Andrews-Hanna & Broquet, 2023), finding that the peak activity could be placed between the late Noachian in to the early Hesperian. The large mass redistribution due to

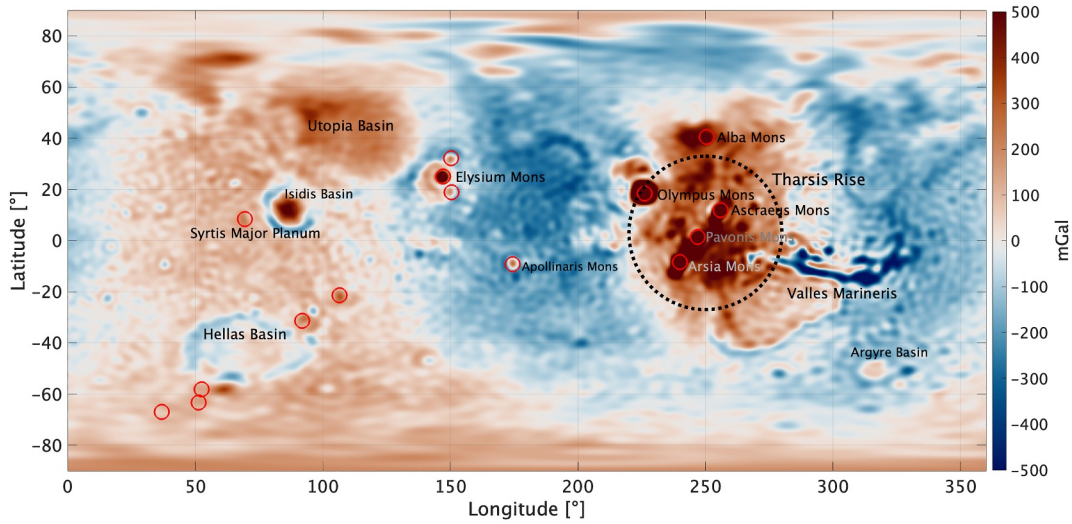

Figure 1. Free-air gravity anomalies of Mars from the JMRO_120d model (Konopliv et al., 2016). The range of the color scale is limited to ±500 mGal in order to show the global feature centered around the Tharsis Region. The maximum gravity anomaly goes up to 3,540 mGal at Olympus Mons (18.65 N and 226.2 E). Major shield volcanoes are depicted by red circles. The Tharsis Region is approximated by the black dashed line (radius of the circle is 28°).

the generation of the Tharsis region has shifted the rotation axis of the planet to find a new rotation equilibrium (Kite et al., 2009). This type of process could explain the apparent migration of Martian volcanism (Zhong, 2009). Furthermore, a displacement of the Martian equator was found by an extensive study of the distributions of the valley network (Bouley et al., 2016), corroborating polar wander. This shows that the Tharsis Region of Mars is probably constructed by vast shield volcanism, inducing differential rotation, followed by other sequences of smaller scale shield volcanism.

The Martian gravity anomalies (Genova et al., 2016; Konopliv et al., 2016; Smith et al., 2001) show a strong correlation with the Tharsis Region (see Figure 1). The center of a positive free-air anomaly (300–500 mGal) after correcting for most of the rotational flattening is centered in between Ascraeus Mons and Pavonis Mons. A pronounced negative gravity ring (−200 mGal) surrounds the bulge of the Tharsis Rise. Antipodal to these volcano regions lie two major impact basins, the Utopia and Hellas Basins. Due to this location, some argue that a huge meteor impact is responsible for the formation and volcanic activity in the Tharsis region (Golabek et al., 2011). Another explanation is that there might be some large underplating of the Martian lithosphere with an anomalous density that is so strong that it can support the region entirely, maybe a remnant of an even larger Borealis impact (Ballantyne et al., 2023). Another explanation could be that an active mantle plume underneath the Tharsis Rise maintains the extreme surface elevation and is responsible for the observed global gravity signal. The idea of a large dynamic plume underneath Tharsis is not new (Harder, 1998; Harder & Christensen, 1996; Kiefer, 2003; Roberts & Zhong, 2007; Schubert et al., 1990; Zuber et al., 2000), but is not widely accepted by the community, as it is proven difficult to generate a large plume in the mantle of Mars. New estimate of the viscosity state of the Martian mantle makes this even more difficult (Plesa et al., 2018).

The geologic findings of Nyquist et al. (2001); Hartmann and Neukum (2001); Neukum et al. (2004); Hauber et al. (2011) show recent evidence of volcanic activity in Tharsis and Elysium provinces in the form of young lava flows. The discovery of a possible mantle plume beneath the region south of Elysium Mons (Broquet & Andrews-Hanna, 2023), gives extra indications that it is possible to have current magmatic activity in the Martian mantle. The global gravity signature located on the Tharsis Rise, depicted in Figure 1, needs a global approach that uses the full range of topographic and gravitational observations. Belleguic et al. (2005) assumed that spherical harmonics degree up to $n = 6$ was mainly due to the Tharsis Rise. This was later corroborated by Beuthe et al. (2012), who found that the Tharsis Rise was seen mainly at long wavelengths ($n = 7$). These long wavelength signals of the gravity field have most sensitivity to deeper regions of the mantle (Martinec, 2014), and could be able to detect any large-scale structure deep beneath Tharsis.

Results from gravitational studies are ambiguous, a fact which keeps the debate about values for average crustal thickness, crustal density, mantle density, and flexure rigidity of Mars ongoing. NASA's Interior Exploration using Seismic Investigations, Geodesy and Heat Transport (InSight) mission has provided new seismological information about the subsurface, particularly in the area south of Elysium Mons (Banerdt et al., 2020). An average crustal thickness between 24 and 72 km is estimated (Knapmeyer-Endrun et al., 2021) from the seismic observations. Slightly larger global crustal thickness are found, between 42 and 56 km by Kim et al. (2023). Furthermore, a seismological lithosphere thickness of 500 ± 100 km was determined by observing a conductive velocity gradient below the crust (Khan et al., 2021). The mission has shown that the iron core of Mars could be still in the liquid phase, as the reflected seismic wave shows clear signs of polarimetric change, which is typical for a liquid reflection (Stähler et al., 2021). With the new seismic constraints of the InSight mission, the value for the crustal thickness beneath the InSight landing site is restricted to around 39 ± 8 km (Wieczorek et al., 2022). These new constraints warrant a reanalysis of the gravitational analysis as it has the potential to reduce the ambiguity in flexure models.

Studies that use topographic and gravitational observations usually follow two distinct approaches (Beuthe et al., 2012; Broquet, Maia, & Wieczorek, 2025). The first is called the classical Bouguer inversion (Zuber et al., 2000): the gravity data are corrected by the gravitational signal of the topography, with a simple or more complex Bouguer reduction in which a particular density is chosen for the topographic mass. The remaining signal is then used to invert for any type of subsurface parameter; most studies focus on the crust-mantle interface or crustal thickness (Goossens et al., 2017; Neumann et al., 2004; Wieczorek et al., 2022; Wieczorek & Zuber, 2004). As a side product, the values for the average crustal thickness and the average crustal and mantle density can be estimated. Sometimes, some varying crustal density linked to a geological interpretation of the crust is inserted to improve the fit for volcanic regions (Goossens et al., 2017) or the dichotomy of Mars (Wieczorek et al., 2022). The drawback of these models is that all other sources that generate gravity anomalies are absorbed by the inversion. Therefore, for example, Wieczorek and Zuber (2004) do not use the gravity signal of degree 10 and lower in order to remove any deep mantle signal in the inversion, as the low degrees would otherwise leak into the crustal thickness estimates. This spectral truncation is useful, but the threshold is often chosen subjectively.

The second approach uses lithospheric flexure theory to construct a model of the lithospheric structure. Flexure theory (Watts, 2001) determines the characteristics of the lithosphere by studying the spectral interplay between topography and gravity and has already been used to study the Tharsis Rise (Audet, 2014; Beuthe et al., 2012; Broquet & Wieczorek, 2019; Ding et al., 2019; McGovern et al., 2002; McKenzie et al., 2002; Turcotte et al., 1981; Zhong & hong, 2002). Phillips et al. (2001) show that flexural lithosphere loading can be considered the main support of Tharsis, following the initial studies by Turcotte et al. (1981). This volcanic loading seems to be already present since the end of the Noachian period (Phillips et al., 2001). Similar findings are obtained by Anderson et al. (2001), Bouley et al. (2018), and J. Andrews-Hanna and Broquet (2023). A reappraisal of flexural theory (Beuthe et al., 2012) reaffirmed that the classical model of the infinite plate fails to take into account the curvature of the planet. Given the relatively smaller size of the planet, the so-called membrane stresses are significant for Mars and are capable of supporting the majority of the volcanic load (Banerdt et al., 1982, 1992). More advanced flexure models include bottom loading, in the form of (sub)crustal density anomalies up to a depth of approximately 420 km (Lowry & Zhong, 2003; Zhong & hong, 2002; Zhong & Roberts, 2003) improving the physical model, but introducing more ambiguity. The contribution of buoyancy forces due to a shallow mantle plume in the upper mantle was found to be small in Zhong and hong (2002). More extensive analysis show that if the plume resides in the shallow part of the upper mantle, it cannot contribute more than 15% to the observed geoid. Therefore, most flexure-only models seem to explain the observed gravity-topography of Mars, supporting a thicker lithosphere underneath the Tharsis region (Broquet & Wieczorek, 2019; Ding et al., 2019). The resulting flexure models would also predict average crustal thickness, crustal and mantle densities, and a value of the rigidity of the lithosphere (usually presented as the elastic thickness parameter T_e) estimates. The drawback of this method is that the flexure models can only give globally constant values for these geophysical parameters.

The spatio-spectral window techniques of Simons et al. (1997) allows for a whole new range of studies where regional flexural analysis is performed to estimate lateral variations in the flexural and subsurface parameters. McGovern et al. (2002); McGovern, Solomon, et al. (2004) use these regional localization techniques to fit the observed admittance, the spectral ratio of topography and gravity, with modeled estimates using flexural methods taking bottom loading into account. Belleguic et al. (2005) revisits most of the previous studies and implemented

a full flexural modeling, applying regional localization techniques. For all models, the load density is constrained to 3,200 ± 100 kg/m^3, suggesting iron-rich basalt, which is in line with volcanic deposits. It becomes clear that models for smaller volcanic regions such as Elysium and Arsia would drastically improve the observational fit by adding subsurface loads (Belleguic et al., 2005). The lighter densities in the mantle below suggest higher temperatures or a more depleted mantle beneath these regions, up to 70 kg/m^3 less than the surrounding mantle. Similar indications for Olympus Mons and Alba Patera are found, but these are less conclusive. The negative densities are interpreted as possible hot mantle plumes. The dynamic bottom loading of Olympus Mons is determined by Beuthe et al. (2012), confirming higher densities of the deposited volcanic rock that formed the Martian volcanoes. The localized spectral admittance approach with studies such as Phillips et al. (2008); Grott and Wieczorek (2012); Broquet and Wieczorek (2019); Broquet and Andrews-Hanna (2023) highlights lateral density changes in the Martian lithosphere. These studies seem to converge and give better insight into the regional structures of Mars and can be used to constrain the thermal evolution of the planet. Despite the success of the regional studies, the origin of the long-wavelength gravitational signal centered at Tharsis keeps being debated as global modeling is needed.

Because of the global nature of the problem, we want to couple the effects of a deep mantle anomaly to a flexural lithosphere model with improved interior estimates from InSight. With this combined model, we can not only determine the uncertainty range in bulk parameters for the lithosphere and crust, but also assess the plausibility of a deep mass anomaly, such as a mantle plume. This approach will be able to utilize the complete topographic and gravity spectrum, without the need for arbitrary filtering of the long-wavelength signal. By constraining our global models to the power spectrum of the gravity observations, we remain sensitive to lateral or regional information, as the remaining residual anomalies can give information in the subsurface lateral density structure of Mars.

In this study, we first discuss the flexural theory that we use to construct a lithosphere for Mars. We present a fast spectral approach that allows us to develop numerous lithosphere models. This is followed by a description of how we obtain the gravity and topographic effect from deep mantle mass anomalies by solving the Stokes/Poisson equations and how to couple this dynamic mantle model to the flexural lithosphere model. A sensitivity study between the degree variance of Martian gravity field data and observed gravity field is used to select the best possible flexure parameters. This flexure model is used to explore the parameter space for the deep mantle anomaly, where we determine possible size, mass and depth of the anomaly. In the last part of the paper, we use residual gravity anomalies inside an inversion algorithm to interpret them as lateral crustal densities. Assessing these density structures gives information about the robustness of the global model and gives new insights in the geological setting of Mars.

2. Martian Data

The subsurface structure of a planet is studied using known information about its topography and gravitational field. We remove the effects of the polar ice caps as we are interested in the subsurface geophysical parameters, such as crustal thickness, density of the crust and mantle, and lithospheric rigidity. In the following subsections we recall the nature of the various data sets that are used in this study.

2.1. Topography Data

The high-resolution global map of the Martian topography was produced by MOLA on the Mars Global Surveyor (Smith et al., 2001). Altimeter data were collected from 1997 to 2001 and can be downloaded from NASA Planetary Data System Geosciences Node (the data was downloaded from https://pds-geosciences.wustl.edu/missions/mgs/megdr.html).

The topography model (Planetary radius minus areoid) based on the MOLA Mission Experiment Gridded Data Records with a global resolution of 16 pixels per degree (Smith, Neumann, et al., 2003) is used. The resolution of these data is already superior to the available gravity field data, and therefore higher resolution topographic data are not needed for this study. The Martian topography is mostly contained between ±5 km, with positive outliers, for example, Olympus Mons (+21.2 km) and negative outliers, for example, inside Hellas basin (−8.2 km).

2.2. Gravity Data

Martian gravity models are derived from precise radio tracking data of satellites, since the orbital dynamics is affected by localized variations of the planet's gravity field strength. From the 1970s to the 1990s, tracking data from Mariner 9, Viking 1 and Viking 2 spacecraft were used to infer the gravity field of Mars, which yielded a maximum degree and order of 50 spherical harmonic solutions (Smith et al., 1993). With additional data from Mars Global Surveyor, Mars Odyssey, and Mars Reconnaissance Orbiter (MRO) since the 1990s, the latest gravity solutions have been improved to degree and order 120.

This study uses the Martian gravity model JMRO_120d (Konopliv et al., 2016) (the model was downloaded from https://pds-geosciences.wustl.edu/mro/mro-m-rss-5-sdp-v1/mrors_1xxx/data/shadr/jgmro_120d_sha.lbl), that was developed by using tracking data from close orbiting satellite missions (Mars Odyssey, MGS, and MRO). We use the spherical harmonics model up to degree and order 90. The model has higher degree coefficients available, but the degree strength of the error surpasses the signal above degree 90. Moreover, for our purpose these higher-resolution data are not making any changes to the conclusions.

To remove most of the equatorial bulge due to the rotation of the planet we set the spherical harmonic coefficient $C_{20} = 0$ for the data as well as in the models. The simplicity of our modeling approach justifies this assumption, but an in-depth study could use the correction proposed by Matsuyama and Manga (2010). Degree 1 gravity signal in our modeling is assumed to be computed by local isostatic compensation of the crust. This seems to work sufficiently well and needs to be done because the flexure modeling and the dynamic mantle models in this study are not able to produce degree one effects. Nevertheless, the degree 1 signal can be a combination of non-isostatic crustal thickness and some degree 1 density distribution, as shown in Wieczorek et al. (2022).

In step one of our modeling approach, we use the degree variance of the Stokes coefficients that represent the gravity field of Mars. The degree variance ($DV(n)$) is defined as follows:

$$DV(n) = \sum_{m=0}^{n} \left(C_{nm}^2 + S_{nm}^2\right) \quad (1)$$

where degree is denoted by n and order is denoted by m. The spherical harmonic coefficients C_{nm} and S_{nm} are squared and then summed up with respect to their order per degree. The model degree variances will be compared to the degree variance of the observations or a part of the degree domain for which certain model parameters are sensitive. For the calculation of gravity anomalies, we use the GSH code (Root, 2021) by Root et al. (2016) and together with the values of $GM = 4.2828372.10^{13}$ m^3/s^2 and $R = 3{,}396.0$ km from the gravity model JMRO_120d of (Konopliv et al., 2016).

2.3. Correcting for the Gravitational Potential and Generate Equivalent Topography for the Polar Ice Caps

Polar ice caps have a different density than that of the average Martian crust. Although the polar cap gravitational signal has limited effect on the global modeling, it still needs to be taken into account in the gravitational signal of the northern and southern polar ice caps and in their loading of the crust. The thickness of the ice caps have been determined with satellite radar sounding instruments. Failing to account for these masses could have an effect on the analysis of any global parameters or apply wrong loading conditions to the Martian lithosphere.

For the southern polar cap on Mars, we use the model developed by Khuller and Plaut (2021b) using Mars Advanced Radar for Subsurface and Ionosphere Sounding (MARSIS) data (Khuller & Plaut, 2021a) on the Mars Express mission from ESA. MARSIS is a radar sounder and altimeter instrument. With its ground-penetrating radar capabilities, it is able to determine the thickness of the southern polar cap on Mars. The southern polar cap thickness model presented in Khuller and Plaut (2021b) is derived from radar data. Together with the topographic data from the MOLA model we determined the top of the ice sheet and the top of the basement (top of the crust).

A model for the geometry of the northern polar cap is obtained from Nerozzi et al. (2022), which is based on Shallow Radar (SHARAD) Sounder data (Nerozzi, 2021). The SHARAD instrument is a radar sounding instrument onboard NASA's MRO. This instrument had ground-penetrating capabilities and was able to determine

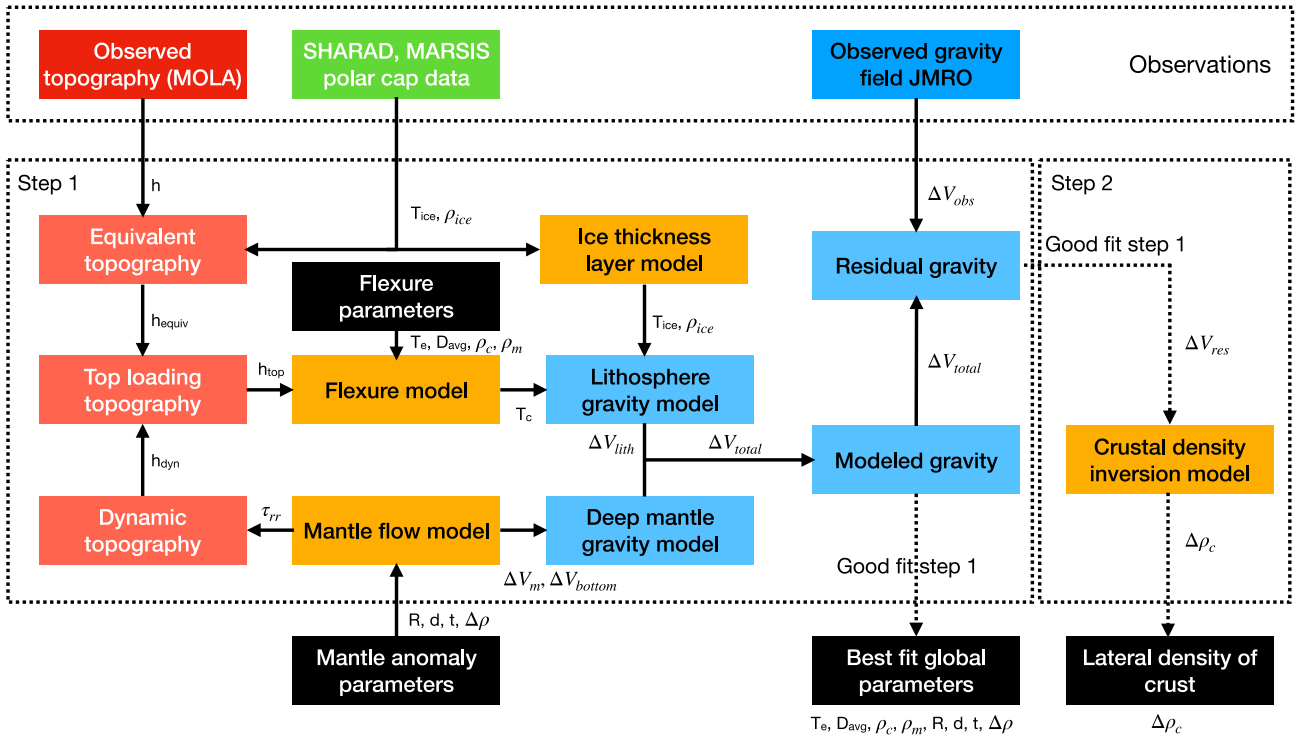

Figure 2. A schematic representation of the modeling approach in this work. The red elements are related to the topography, blue elements are related to the gravity field, green elements are related to the polar ice caps, and yellow elements depict the different numerical models that will be explained in Sections 2.1 and 2.2. Black elements are related to the model parameters that are main outcomes in this research.

the thickness of the northern polar cap. Here, we use the model by Nerozzi et al. (2022) of the basement unit to separate the ice mass from the MOLA data. Our obtained polar ice sheet thickness models are approximately similar to Broquet et al. (2020, 2021).

From the SHARAD and MARSIS based models of the northern and southern polar ice cap geometries, we compute the gravitational field of the caps using a density of 1,220 kg/m^3, following Zuber et al. (2007). This value, higher than pure H_2O ice density, is justified by the presence of solid CO_2 and dust. These values also fall within the uncertainty limits of the estimates in Broquet et al. (2020, 2021). We are able to compute the full gravitational field of our model by adding the polar gravitational potential to the modeled crustal and mantle layers.

To correct for the reduced surface load (the ice density is lower than the crust density), an equivalent topography (h_{equiv}) is calculated (Hirt et al., 2012). Equation 2 depicts how the equivalent topography is calculated for the polar ice caps:

$$h_{equiv} = h_{basement} + T_{ice}\frac{\rho_{ice}}{\rho_c} \tag{2}$$

The crustal density (ρ_c) and the ice density (ρ_{ice}) are used together with the thickness of the ice sheet (T_{ice}) to calculate the equivalent topography at the area where there is an ice sheet.

3. Martian Gravity Field Modeling

To model the gravity field of Mars we have coupled a lithospheric flexure model with a dynamic mantle code. We first discuss both methodologies separately and then describe how to couple them in a consistent manner. The resulting crust and mantle structure are then forward modeled to predict their gravitational signal, such that this can be compared to the observed gravity field of Mars. The residual gravity anomalies are used in a second step that inverts for crustal density. A schematic overview of the procedure is presented in Figure 2, where we shown

how the data is used in our two-step modeling approach. The results are the best fitting parameters for lithospheric flexure and a deep mantle anomaly, plus lateral varying density of the Martian crust.

3.1. Lithospheric Flexure Model

To start the lithosphere modeling, the Airy isostasy equation is used to determine an initial crust-mantle geometry. The deviation of the root r of the crust-mantle boundary with respect to the average crustal thickness can be computed from the topography h:

$$r(\theta,\lambda) = \frac{\rho_c}{\rho_m - \rho_c} h(\theta,\lambda) \tag{3}$$

where ρ_c and ρ_m are the density of the crust and the mantle respectively, both at latitude θ and longitude λ. The root needs to be added to a chosen reference thickness of the crust (D_{avg}) to obtain the depth of the crust-mantle interface:

$$d(\theta,\lambda) = D_{avg} + r(\theta,\lambda) \tag{4}$$

The depth of the crust-mantle interface can then be calculated for any latitude θ and longitude λ. This assumption of local compensation neglects the shear stresses between the crustal columns and only relies on the buoyancy to provide support. The topography is mapped one-to-one to the crust-mantle boundary, causing unrealistically large amplitude geometric features. The average crustal thickness (D_{avg}) should be chosen carefully, since too low a D_{avg} can cause a negative crustal thickness in the Hellas Basin. In light of this we have therefore set a lower bound to D_{avg} of about 45 km for all other density and elastic thickness models.

For a thin shell with radius R_m and a uniform thickness of T_e, Kraus (1967) derived the vertical displacement or deflection w under surface loads. This was later corrected by Beuthe (2008) as a term was missing in the original equation. This approximation takes into account the membrane stresses in the curved lithosphere and leads to

$$\left[D\nabla^6 + 4D\nabla^4 + \left(4D + R_m^2 E T_e\right)\nabla^2 + 2R_m^2 E T_e\right] w = R_m^4 \left(\nabla^2 + 1 - \nu\right) p, \tag{5}$$

where w is the deflection of the lithospheric plate. D is called the flexural rigidity which is given by

$$D = \frac{E T_e^3}{12(1-\nu^2)}. \tag{6}$$

where E is the modulus of elasticity (or Young's modulus) and ν is Poisson's ratio. T_e is the effective elastic thickness of the lithosphere, which describes the lithosphere's resistance to bending or deflection under vertical loads. A higher effective elastic thickness represents a more rigid lithosphere, resisting bending. In Equation 5 the Laplacian operator is represented by ∇^2, which in the spherical harmonic domain becomes $-n(n+1)$ and p is the loading pressure, defined as follows:

$$p = g\left[\rho_c h - \left(\rho_m - \rho_c\right) w\right]. \tag{7}$$

This approach neglects self-gravity and assumes that the gravity is constant for all loading mass. Sensitivity studies are described in the (Figures S4, S5, and S6 in Supporting Information S1), and show that second-order effects will not change the main conclusion of this study. The assumption of constant gravity has less than 10 percent effect at Mons Olympus and much lower in other parts of Mars. The self-gravitation mostly affects the results at the large impact basins (5–15 km less thick crust), which need more sophisticated modeling compared to our global flexure modeling. Due to the computational inefficiency and the low impact on the conclusions, we will not take into account these second order effects.

The reader is referred to for example, Beuthe (2008) for a more complete derivation of Equation 5. Eventually, the equation can be formulated in the form of a flexural response function:

$$\Phi(n)_{shell} = \left[1 + \frac{D}{(\rho_m - \rho_c)g}\left(\frac{1}{R_m^4}\frac{[n(n+1)-2]^2}{1-\frac{1-\nu}{n(n+1)}} + \frac{12(1-\nu^2)}{T_e^2 R_m^2}\frac{1-\frac{2}{n(n+1)}}{1-\frac{1-\nu}{n(n+1)}}\right)\right]^{-1}. \quad (8)$$

The curvature of the lithosphere increases the complexity of the equation with respect to the infinite plate assumption. Notice the scaling factor F_{flex} defined as:

$$F_{flex} = \frac{D}{(\rho_m - \rho_c)\, g} \quad (9)$$

It contains all the modeling parameters and is mostly responsible for how the elastic rigidity D and the buoyancy pressure is providing support for the topography. We will later use this parameter to understand the ambiguity of the elastic thickness and mantle density parameters.

The flexural response function is used to modify the Airy model from Equation 4 to construct a flexure-derived crust-mantle interface. In order to use the flexural response function, the crust-mantle boundary needs to be decomposed in the spherical harmonics domain:

$$d(\theta,\lambda) = \sum_{n,m} P_{nm}(\sin\theta)(A_{nm}\cos(m\lambda) + B_{nm}\sin(m\lambda)). \quad (10)$$

The spherical harmonic coefficients A_{nm} and B_{nm} can then be multiplied by the flexural response function $\Phi(n)$:

$$M_{nm} = A_{nm}\Phi(n) \quad (11a)$$

$$N_{nm} = B_{nm}\Phi(n) \quad (11b)$$

By multiplying A_{nm} and B_{nm} with the flexural response function, M_{nm} and N_{nm} become the new coefficients for the crust-mantle boundary. These coefficients need to be transformed back into the spatial domain to obtain the geometry of the flexure-derived crust-mantle interface. This approach allows for a fast forward modeling of the interface, such that a large range of flexure parameters can be explored.

3.2. Deep Dynamic Mantle Model

The flexural methodology focuses solely on the top loading of the lithosphere and does not take into account the signal coming from the deep mantle. Here, we discuss how to compute the topographic and gravity effect of deep mantle anomalies. At first sight, a positive density anomaly generates a positive gravity signal and a negative density anomaly generates a negative signal. However, a positive density anomaly also causes a downward flow that affects the top and bottom boundaries of the mantle shell, the core-mantle boundary (CMB). This flow results in dynamic pressure at the top boundary of the mantle (e.g., the lithosphere) and at the CMB. The deflection of these boundaries compensates the gravity signal coming from the mass anomaly, reducing the overall magnitude of the varying gravity field. Consequently, the dynamic boundary variation, dynamic topography and dynamic CMB topography need to be modeled to fully reproduce the observed gravitational effect of the deep mantle.

To calculate the dynamic stress at the bottom of the lithosphere, the gravity contribution from the sub-lithospheric mantle, and its boundary deflection at the CMB, the Stokes-Poisson equations for an incompressible viscous shell are considered (Tosi, 2008). Steinberger and Antretter (2006) showed that there is little difference between compressible and incompressible predicted dynamic topography of present-day mantle flow to warrant this modeling assumption.

Table 1
Summary of Parameters for the Mars Modeling

Parameters	Symbol	Parameter range	Selected model (d/o 2–8)	Units
Gravitational constant	G	6.67×10^{-11}		$m^3/kg/s^2$
Model radius	R_{Mars}	3,396.0		km
CMB radius	R_{CMB}	1,561.0		km
Gravitational acceleration	g	3.72		m/s^2
Poisson's ratio	ν	0.30		–
Young's modulus	E	100		GPa
Crustal thickness	D_c	45 - 85	55	km
Crustal density	ρ_c	2800 - 3200	3,050	kg/m^3
Crust-Mantle contrast	$\Delta\rho = \rho_m - \rho_c$	100–1,000	700	kg/m^3
Elastic thickness	T_e	45–150	100	km
Mantle anomaly radius	R	1,100–2000	1,500	km
Mantle anomaly thickness	t	50–400	400	km
Mantle anomaly density	$\Delta\rho$	−100–−10	−60	kg/m^3
Mantle anomaly depth	d	800–1,600	1,200	km

Note. The values in the table are used in this study unless otherwise specified.

$$0 = \nabla \cdot \mathbf{u} \tag{12}$$

$$\mathbf{0} = \nabla \cdot \boldsymbol{\tau} + \rho_0 \nabla V - \mathbf{g}_0 \delta\rho \tag{13}$$

$$\boldsymbol{\tau} = -p\mathbf{I} + 2\eta\dot{\boldsymbol{\varepsilon}}(\mathbf{u}) \tag{14}$$

$$\nabla^2 V = 4\pi G \delta\rho \tag{15}$$

In these equations, $\mathbf{u}$ is the velocity, $\boldsymbol{\tau}$ is the stress tensor, $\rho_0(r)$ is the radial average density, $\delta\rho(r,\theta,\lambda)$ the density anomalies with respect to that average value. The average gravitation is given by $\mathbf{g}_0$ and the gravity anomalies δg can be calculated with $\delta g = -\nabla V$. The stress $\boldsymbol{\tau}$ is a function of the internal pressure p, the effective viscosity η and the strain-rate tensor $\dot{\boldsymbol{\varepsilon}}(\mathbf{u})$.

We prescribe free-slip boundary conditions on the top and bottom boundary of the spherical shell. The system of coupled PDEs is solved numerically with a spectral finite element code (SFEC) (Reusen et al., 2020; Tosi, 2008). SFEC calculates the solution for degree and order 2 until 10 while degree 0 and 1 signals are not calculated for the dynamic part. Higher degrees of the dynamic signal are not significantly contributing to the observed gravitational signal because of the large size and depth of the density anomaly in the mantle.

The dynamic topography results from the assumption that the calculated radial stress τ_{rr} on the boundaries would be balanced by the pressure force of the displaced topography or the CMB undulations ($h_{dynamic}$). These displacements are calculated at each point of the surface and CMB as follows:

$$h_{dynamic} = -\frac{\tau_{rr}}{\Delta\rho_0 g_0} \tag{16}$$

where the density contrast $\Delta\rho_0$ is the density contrast between the Martian mantle with the air or core densities. A typical result (selected flexure model; see the numerical values in Table 1) for the dynamic topography is seen in Figure 4, which can go up to 1 km on Mars. Furthermore, the code computes the gravitational potential of the internal density variations. Then, both signals (V_{top} and V_{bottom}) are usually added to the internal mantle gravitational signal (V_{mantle}). These three components make the total gravity signal (Hager & O'Connell, 1981). In order to account for our flexure lithosphere model, we separate the top boundary effect from the internal mantle and bottom boundary effect (Reusen et al., 2020). We use the dynamic topography $h_{dynamic}$ to correct the observed

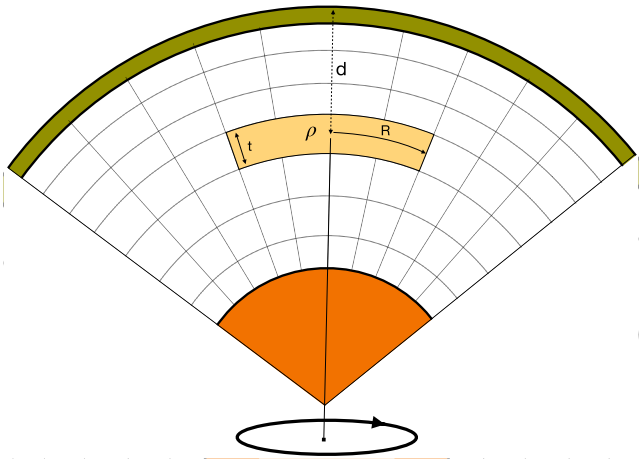

Figure 3. Sketch of the mantle anomaly in a cross-section of an axisymmetric conical shell. The structure can be parameterized by four values: the radius of the mass anomaly at mid-point (R), the thickness of the disk (t), the density contrast ($\Delta\rho$), and the depth of the center of the disk (d). This anomaly is inserted in the spectral finite element code code (Reusen et al., 2020; Tosi, 2008) to compute the resulting surface stresses and the resulting dynamic topography. The green layer is an elastic lithosphere and the orange is the core of the planet, which is not modeled.

topography and use the residual topography for the flexural modeling. Section 2.3 elaborates further on how to combine the gravitational signal of the mantle convection models with the flexural models.

The input for the mantle convection code SFEC (Tosi et al., 2024) consists of a geometry, a 3D density field, and a 1D radial viscosity profile of the mantle shell. The outer radius of the shell is set to 3,396 km to comply with the value used in the gravity field model (Konopliv et al., 2016) and we use the latest estimates from the InSight mission, setting the inner radius (CMB) to 1,835 km (a depth of 1,560 km) (Stähler et al., 2021). We assume this inner boundary to be a solid-to-liquid interface and is able to deform. A solid iron core would resist the stresses of mantle convection more, that would result in $h_{bottom} = 0$.

In this study, a single mass anomaly in the mantle is modeled to represent a large mass structure. This is parametrized by a circular spherical body with thickness t, a radius R, a density anomaly ρ, and depth of the center of the body d. A sketch of the mass anomaly parameterization is shown in Figure 3. The lateral resolution is chosen such that the radius of the disk is approximated within the desired precision (less than 1 mGal error at the surface). An overview of the values for the parameters is given in Table 1.

The viscosity profile used in this study is a simplified 4 layer model based on Steinberger et al. (2010). We approximate this model by having four layers: the crust ($\eta_l = 10^{23}$ Pa.s), the lithosphere ($\eta_l = 10^{23}$ Pa.s), the upper mantle ($\eta_{um} = 6 \times 10^{20}$ Pa.s), and lower mantle ($\eta_{lm} = 10^{21}$ Pa.s). The viscosity of the lithosphere is much lower than found by InSight results, but we found that if the lithosphere viscosity is 2 orders of magnitude higher than the upper mantle, the layer is acting as an elastic layer. Increasing the viscosity in SFEC will not change the results, but will introduce numerical issues that require higher radial resolution, increasing the computation time. The thickness of the lithosphere in the dynamic modeling is set to the values of elastic thickness T_e used in the flexure model. The boundary between the upper mantle and lower mantle is set to a depth of 500 km (radius of 2,896 km) to reflect the seismological change seen by InSight (Khan et al., 2021). We do not focus on a thorough viscosity parameter search in this study, but future work should investigate the sensitivity of the results to the viscosity structure.

3.3. Combining Deep Mantle to Flexural Theory

To get a full model of the Martian gravity field, the gravity effect of the deep mantle and the lithosphere model constructed by flexural theory are combined in a consistent manner (Reusen et al., 2020). In reality the observed

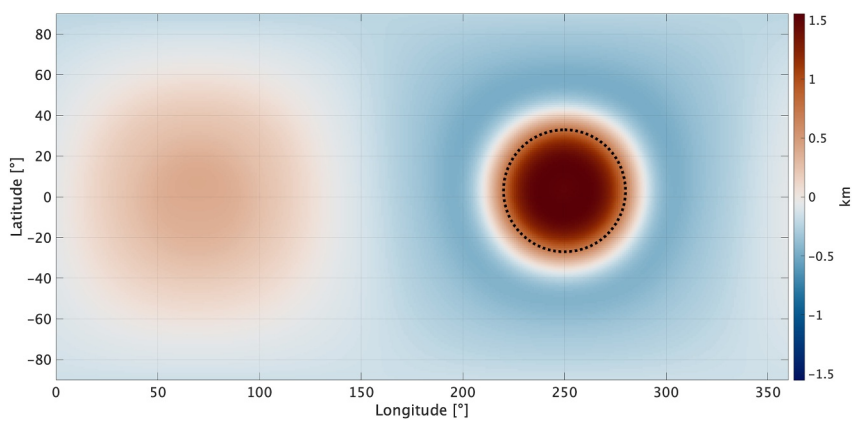

Figure 4. The dynamic topography signal from the selected model. This signal is derived from the density anomaly in the deep mantle by solving the Stokes equations (Equation 12) and Equation 16 based on the selected model geometries. The corresponding size of the deep mantle density anomaly is denoted by the dashed line.

topography is made by two signals, the dynamic topography and the top loading topography. The dynamic topography (h_{dyn}) is calculated using the SFEC (Tosi et al., 2024) code (Tosi, 2008) as explained in Section 2.2. The top loading topography (h_{top}) can be determined subtracting the dynamic topography from the observed topography.

$$h_{top} = h_{obs} - h_{dyn} \tag{17}$$

This top loading topography is used in the flexural modeling, starting by calculating a crust-mantle interface with Equation 3.

The gravitational signature of these lithosphere models is computed using the Fast Spectral Methodology described in Root et al. (2016). The lithosphere gravity field is determined from the layered 3D density model based coefficients V_{nm}:

$$V_{lithosphere} = \frac{GM}{R_{Mars}} \sum_{n,m} \left(\frac{R}{r}\right)^{n+1} \left(V_{nm}\ \bar{Y}_{nm}\right). \tag{18}$$

The corresponding coefficients V_{nm} are multiplied with the associate Legendre functions $\bar{Y}_{nm}$ to synthesize the fields back into the spatial domain. For a mathematical overview, we refer the reader to Novák and Grafarend (2006) and Root et al. (2016). The lithospheric gravity signal $V_{lithosphere}$ should be added to the deep mantle gravity effect V_{mantle} and the gravity effect of dynamic undulations at the CMB (V_{bottom}) as follows:

$$V_{total} = V_{lithosphere} + V_{mantle} + V_{bottom}. \tag{19}$$

The combined gravity field can then be compared to the degree variance of the observed gravity field (Konopliv et al., 2016).

3.4. Sensitivity Analysis of the Model Parameters

Four different variables can be varied in the flexure model: the crustal thickness D_{avg}, the crustal density ρ_c, the mantle density (or density contrast at the crust-mantle interface) $\Delta\rho$, and the elastic rigidity (or elastic thickness if the bulk modulus is kept fixed) T_e of the lithosphere (Broquet & Wieczorek, 2019). All other parameters in the model are relatively well constrained and can be found in Table 1. Other studies, like Taylor et al. (2020), have taken more parameters into account, but we believe that the available data does not justify the use of more model parameters for global studies. In the majority of Mars studies, parameters pertaining to the gravity modeling are fitted to an arbitrary set of spherical harmonics, or spectral domain, to reduce the ambiguity that gravity models have for different depths. For example, Wieczorek and Zuber (2004) remove the first 10° that would eliminate any mantle signals, and McKenzie et al. (2002) use different bandwidths to compare the flexure models with the observed admittance. These choices of bandwidth might introduce unwanted subjectivity in the model results. We therefore perform a spectral sensitivity analysis to determine the spectral domain in which D_{avg}, ρ_m, ρ_c, and T_e are the most sensitive in flexural studies. We vary the parameters as follows: the crustal thickness between 20 and 140 km with steps of 20 km, the crustal density between 2,600 and 3,300 kg/m^3 with steps of 100 kg/m^3, the mantle density contrast between 100 and 1,000 kg/m^3 with steps of 100 kg/m^3, and the elastic thickness between 30 and 230 km with step sizes of 20 km.

Figure 5 presents the sensitivity of the four model parameters to the gravity field for the thin shell flexure model, by showing the normalized degree variance $DV^{normalized}(n)$ of the observed and modeled gravity field calculated as follows:

$$DV^{normalized}(n) = \frac{DV^{modeled}(n)}{DV^{observed}(n)}. \tag{20}$$

The normalized observed gravity degree variance is one for all degrees. For the modeled normalized degree variance plots, we vary one parameter in the flexural model, while keeping the others fixed. The crustal thickness variations show to have no sensitivity in the short wavelength regime (above 30° and order (d/o) of the spherical

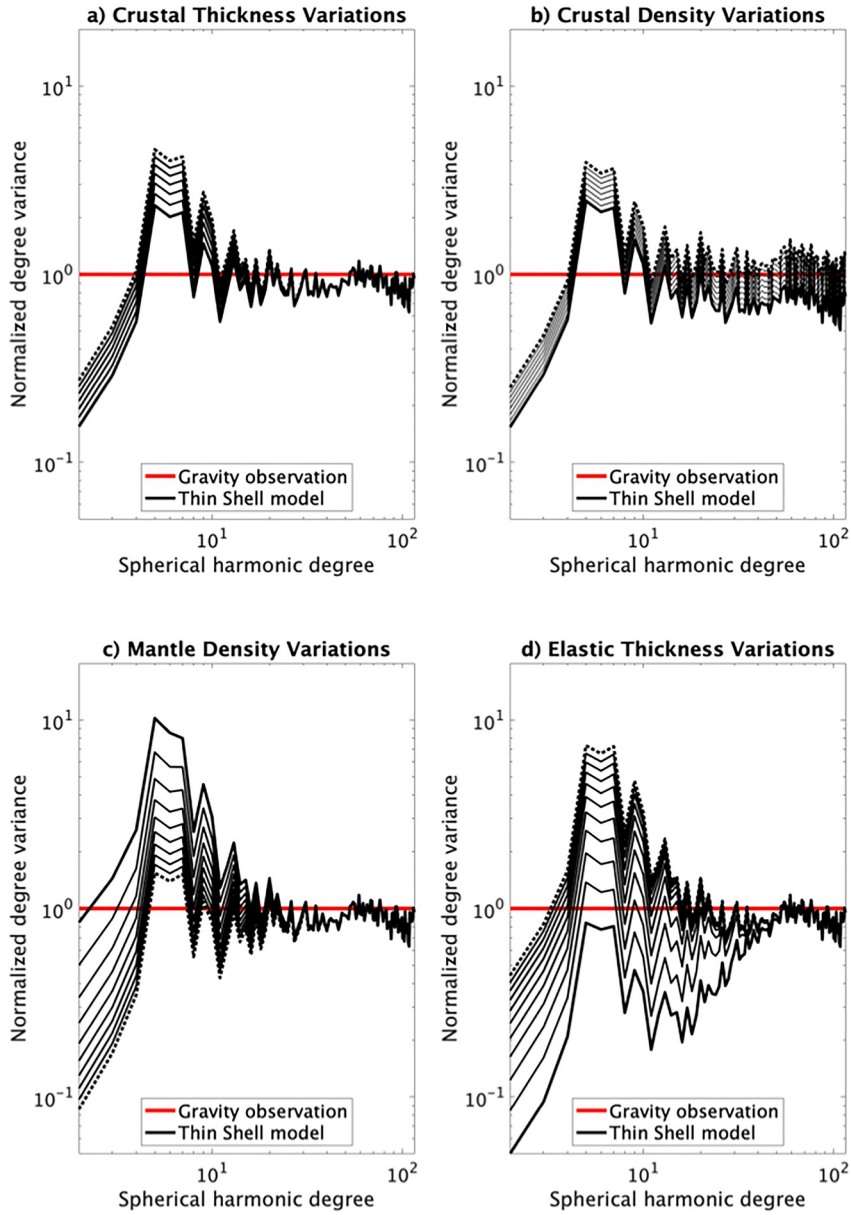

Figure 5. Sensitivity analysis of the thin shell model parameters. The degree variance is normalized by the observed gravity field degree variance. (a) the crustal thickness is varied (20–140 km with step size of 20 km). (b) the crustal density is varied (2,600–3,300 kg/m^3 with step size of 100 kg/m^3). (c) mantle density contrast is varied (100–1,000 kg/m^3 with step size of 100 kg/m^3). (d) the elastic thickness is varied (30–230 km with step size of 20 km). The default values for the other parameters are: crustal thickness $D_c = 60$ km, crustal density $\rho_c = 2{,}900$ kg/m^3, mantle density contrast $\Delta\rho = 500$ kg/m^3, and elastic thickness $T_e = 100$ km. The thick black line denotes the lowest value and the dotted black line the largest value of the parameter range.

harmonic domain). The small sensitivity to the crustal thickness is mainly due to the new information from the InSight mission south of Elysium Mons. This drastically reduces the variability of the average crustal thickness parameter for the thin shell model to 39 ± 8 km at InSight landing site (Wieczorek et al., 2022). The crust-mantle density contrast and the elastic thickness are most sensitive in the spectral domain between 2 and 30 d/o and also show limited sensitivity for signals above 30 d/o. The crustal density seems therefore to be the only parameter that is affecting the short-wavelength regime of the gravity field. This means that observed short-wavelength (larger than 30 d/o) gravity anomalies can be used to estimate the average crustal density of Mars for our given set of investigated parameters.

In the long- and mid-wavelengths (d/o 2–30), the elastic thickness and the crust-mantle density contrast show relatively more sensitivity to the gravity field than the crustal thickness. Looking at Equation 8, these two parameters are inversely proportional to each other, and a saddle curve equilibrium is expected to find the best fitting parameters. The crust-mantle density contrast is less well constrained, about 200–1,000 kg/m^3. Similarly, the elastic thickness is modeled between 0 and 300 km. Yet, all these parameters are not able to capture the distinct pattern of the observed degree variance between degree 2–6; when the flexure model fits degree 2–3 it overestimates degree 4–6, and when it fits to degree 4–6 it underestimates degree 2–3. We conclude that *a flexural lithosphere model, with top-loading only and globally constant crustal thickness and lithosphere rigidity, is not able to completely describe the Martian gravity field*. This could support our hypothesis that *a (deep) large scale density anomaly is partly responsible for the strong gravity signal in the long wavelength regime*.

In light of this, we also performed a sensitivity study on the gravity field for its sensitivity to the deep mantle anomaly parameters. The density anomaly is characterized by its depth d, radius R, density contrast ρ (with respect to the surrounding mantle), and thickness t (see Figure 3).

Figure 6 shows the gravity sensitivity to the parameters of the deep mantle anomaly. The most striking observation is that the dynamic mantle signal only affects the gravity field up to 8 d/o. This is interesting because the flexural parameters can then be determined using the spectral domain above degree 8 without being biased by the dynamical signal. However, in practice local flexural parameters depend on the dynamic signal from the mantle, as a warm plume implies a thinner lithosphere underneath Tharsis. The depth and thickness of the disk give similar sensitivities. However, the thickness of the disk produces slightly larger signals in degrees 5–8 of the gravity spectrum, making the spectrum a bit more flat with respect to the spectrum due to depth variations. The size of the disk (radius) seems to be mainly affecting the gravity spectrum below degree and order 5. The effect of the radius of the disk captures the strong decline of the degree variance from degree 2–3 to higher degree and order coefficients. The other parameters are not able to show such a strong decline in the spectral power from degree 3, as their effect shows a more constant shift in degree variance over the whole spectrum.

3.5. Lateral Density Variations in the Crust

In the first step of our modeling, we fit the flexure and deep mantle parameters to the degree variance of the gravity field. Even when the best misfit is found, there remain substantial gravity anomalies that reflect the assumptions of our modeling due to the choice of global homogeneous parameters for the crust and mantle. Therefore, in a second step, we choose to invert the remaining gravity residual for lateral varying crustal densities. We can then assess whether our global model does generate unrealistic crustal density variations or not. Comparing these variations with the regional geology of Mars could give insight into the usefulness of the global model.

With a simple linear inversion, the lateral densities are determined in the following iteration:

$$\rho^{i+1}_{crust}(\theta,\lambda) = \rho^{i}_{crust}(\theta,\lambda) + SF \cdot \Delta g^{i}_{res}(\theta,\lambda) \tag{21}$$

During the first iteration, the initial density is set to the homogeneous crustal density used in the flexure model (ρ_{crust}). The residual gravity signal between observed and modeled gravity is multiplied by a scaling factor SF to generate a heterogeneous density. This new laterally varying density is inserted in the flexure model, and a new modeled gravity field is obtained. This is repeated (around 20 times) until the inversion converges and the residual gravity signal approaches zero (<1 mGal). The scaling factor is chosen such that the iterative approach does converge: in our modeling it is set to 0.35, which yields a convergence of the RMS residual after 15 iterations.

Neumann et al. (2004) developed a crustal model, in which the volcanic regions received a higher density than the surrounding crustal rock. The volcanic regions are considered to be 600 kg/m^3 denser than the bulk density of the crust to improve the gravity fit of the model. Short wavelength spectral analysis of the observed gravity field showed equivalent crustal density variations between 1,800 and 3,200 kg/m^3, which are indicative of lateral density variation, but due to the low gravity resolution no robust results could be obtained (Goossens et al., 2017). Goossens et al. (2017) proposed to model the major volcanic regions with densities that are 350 kg/m^3 above the bulk density value. Wieczorek et al. (2022) studied the effect of density differences between the northern and southern hemispheres, implementing a density difference of around several 100 kg/m^3, with lower densities for

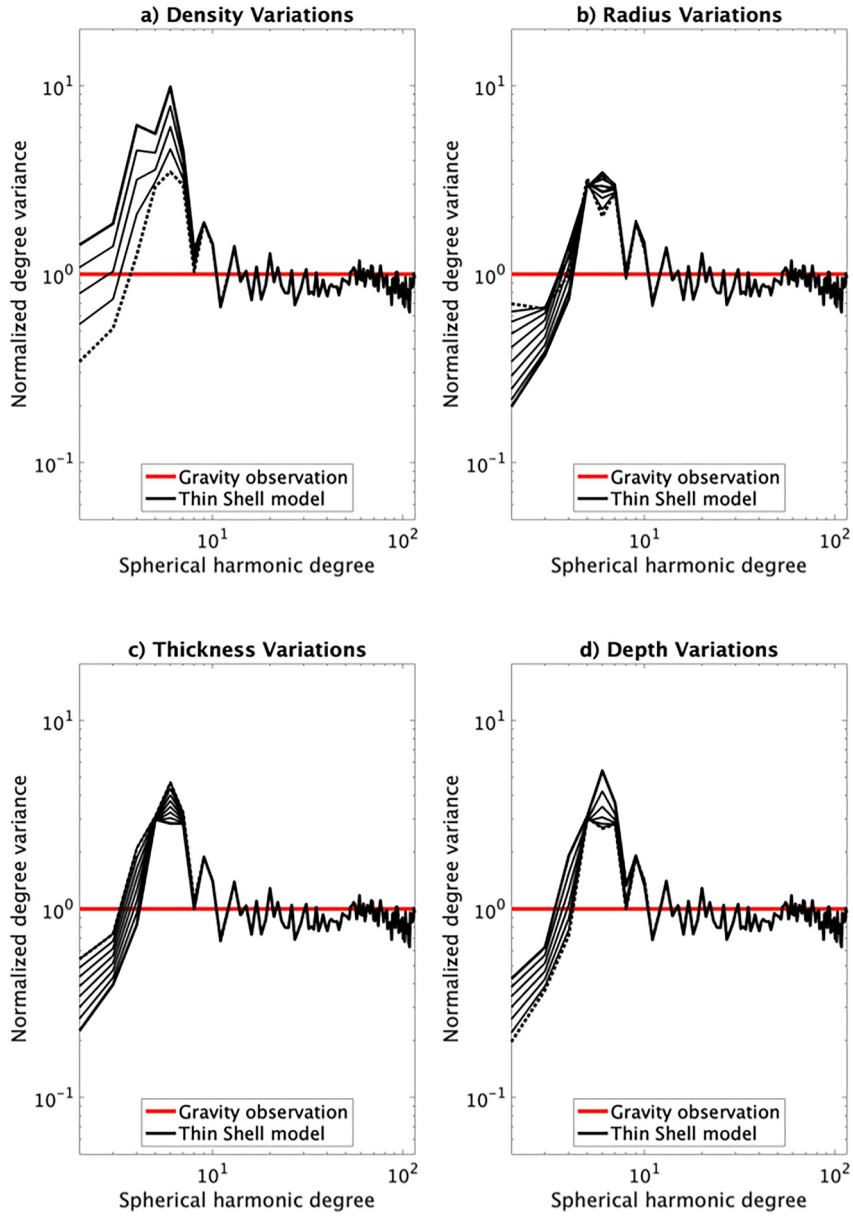

Figure 6. Sensitivity analysis of the normalized degree variance to mantle upwelling results for the mantle anomaly. (a) the disk density is varied (−50 to −250 kg/m^3 with step size of 50 kg/m^3). (b) the disk radius is varied (200–2,000 km with step size of 200 km). (c) the disk thickness is varied (40–220 km with step size of 20 km). (d) the depth is varied (400–1,600 km with step size of 200 km). The default values for the other parameters are: disk density $\rho_{disk} = -50$ kg/m^3, disk radius $R = 1{,}000$ km, disk thickness $t = 100$ km, and disk depth $d = 800$ km. The thick black line denotes the lowest absolute value and the dotted black line the largest absolute value of the parameter range.

the southern hemisphere. Regional analysis of the gravity signature of the Martian volcanoes (Broquet & Wieczorek, 2019) showed crustal densities varying between 2,920 and 3,350 kg/m^3. If our global model is realistic, crustal densities should not vary more than several 100s kg/m^3, when inverted from the residual gravity signature.

4. Results

We have run two sets of models: a flexure-only model set and a full model set (which combines the flexure models with mantle convection of a deep mantle mass anomaly). The sensitivity study in Section 2.4 showed that the

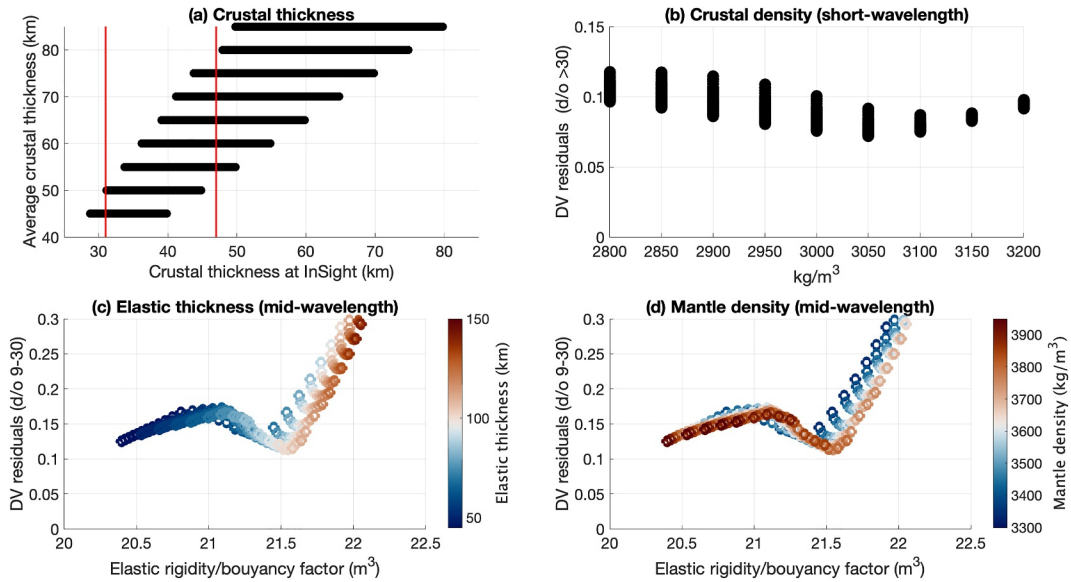

Figure 7. Fitting values (RMS) of the flexure-only models to the observed gravity degree variance. (a) The crustal thickness fitted using the mid-wavelength (SHC 9–30) of the gravity field. The red lines are the crustal thickness estimates of Knapmeyer-Endrun et al. (2021) at the InSight landing site. The color scale is the crustal thickness. (b) The crustal density fitted using the short-wavelength (SHC 31–90). (c) The mantle density parameter fitted using the mid-wavelength (SHC 9–30), and (d) the elastic thickness fitted using the mid-wavelength (SHC 9–30). The bottom sub-figures use a subset of the sensitivity results, where the crustal thickness is 55 km and the crustal density is 3,050 kg/m^3.

optimization of the flexure parameter can be decoupled from the parameters of the deep mantle by fitting to different parts of the spherical harmonic spectra. The mantle convection parameters are only sensitive to the first 8° spherical harmonic coefficients of the gravity field. The rest of the gravity field can be used to explore values for the flexure parameters.

4.1. Flexure-Only Models

The optimization results of these flexure-only experiments (without modeling the mantle dynamics) are presented in Figure 7. In Figure 7a, the resulting crustal thickness at the InSight landing site is plotted for a certain average crustal thickness.

The average crustal thickness of Mars was reported to be between 24 and 72 km by Knapmeyer-Endrun et al. (2021), where their thick-crust model seems to be between 40 and 72 km. This seems to be more in line with our modeling, as the thin-crust model reported 24–39 km global crustal thicknesses, and these are not feasible in our flexural modeling. The thick-crust model of Knapmeyer-Endrun et al. (2021) sees a crustal thickness underneath the Insight lander of 39 ± 8 km, which we use to refine our crustal thickness estimate. Kim et al. (2023), found average crustal thickness values ranging between 42 and 56 km. Our modeling shows that only crustal thickness above 45 km seems to be physically possible for a realistic range of the other flexural modeling parameters. Lower values will introduce negative crustal volumes at Hellas basin and Isidis basin. The crustal thickness results in Figure 7a show no preference for any value between 50 and 55 km. Certain models using 45 and 60 km under- or overestimate the crustal thickness at InSight. We conclude that the average crustal parameter (D_c) should lie in the range of 55 ± 10 km. For all the models later in this study, a value of 55 km is selected as it allows to study a larger range of deep mantle parameter values, than a smaller average crustal thickness.

Figure 7 also shows the standard deviation of the degree variance residuals for a selected bandwidth. Degree and order values higher than 30 are used for the crustal density and degree and order values between 9 and 30 are used for the mantle density and elastic thickness parameters. The sensitivity study in Section 2.4 showed that the average crustal density can be decoupled from the other model parameters, by using the short wavelengths of the gravity field. Figure 7b shows the short-wavelength (d/o >30) degree variance residuals with respect to the crustal

Table 2
Crustal Thickness and Spectral Domain Sensitivity Analysis for Selecting the Best Elastic Thickness (T_e) and Mantle Density (ρ_m) Values

	Best fit d/o 9–30	Best fit d/o 15–30
D_c (km)	T_e (km) and ρ_m (kg/m^3)	T_e (km) and ρ_m (kg/m^3)
45	80–3,500	70–3,300
50	100–3,750	75–3,350
55	115–4,000	80–3,400
60	120–4,050	90–3,500
F_{flex} (m^3)	3.3981 10^{21}	3.1623 10^{21}

density parameter. The best fitting crustal density appears to be 3,050 kg/m^3. The spread in the points is due to the range of other parameters.

As we have seen in Section 2.4, the mid-wavelength regime (9–30 d/o) of the gravity field is sensitive to the mantle density and the elastic thickness and less sensitive to crustal thickness. The crustal density is already independently determined and the dynamical mantle signal is not sensitive to that part of the gravity field spectrum. Figures 7c and 7d show the residuals for the gravity field anomalies and degree variance for the (9–30) part of the spectrum. We find that the best fitting model has an elastic thickness of 100 km, with a corresponding mantle density of 3,750 kg/m^3. We performed a robustness analysis to see the effect of choosing 55 km for the averaged crustal thickness. Table 2 shows that reducing or increasing the crustal thickness has a slight effect on the best fitting parameter values. An increase in crustal thickness will increase the value for elastic thickness and mantle density, and a reduction in crustal thickness will reduce the values of these parameters. Figures 7c and 7d shows another local minimum, slightly worse fitting to the gravity field. These models work best for a low elastic thickness and high mantle density, which illustrates the need for more localized compensation. This is necessary because the degrees 9–14 are dominated by the wavelengths of the large impact basins, like Hellas, Utopia, and Argyre. By using the spectral bandwidth of degree and order 9–30 this set of models tends to overpower the global fitting, favoring low elastic thickness values. When we reduce the bandwidth and only use degree and order 15–30 for the fitting of the elastic thickness and mantle density, this extra local minimum in the residual plots disappears. Furthermore, the effect of the uncertainty in crustal thickness is also reduced (See Table 2). The F_{flex} value also reduces from 3.981 to 3.1623 10^{21} m^3 after removing the long-wavelength signals in the fit.

The F_{flex} factor nicely illustrate the relationship of the elastic thickness and the mantle density. The best fitted models for different T_e and ρ_m in Figure 8, seem to lie on the same value for F_{flex} = 3.3981 10^{21} m^3 for models with crustal thickness of 55 km. This ambiguity clearly explains why gravity alone cannot come up with a consistent elastic thickness (T_e) and mantle density (ρ_m) values. The Insight mission did drastically reduce the ambiguity of the average crustal thickness, allowing to determine the average crustal density and an optimal value for F_{flex}. A combination of the T_e and ρ_m parameters in the form of F_{flex} (Equation 9) does have a single minimum in the gravity residual plot. We select the following scenario for the further modeling with the dynamic signal in

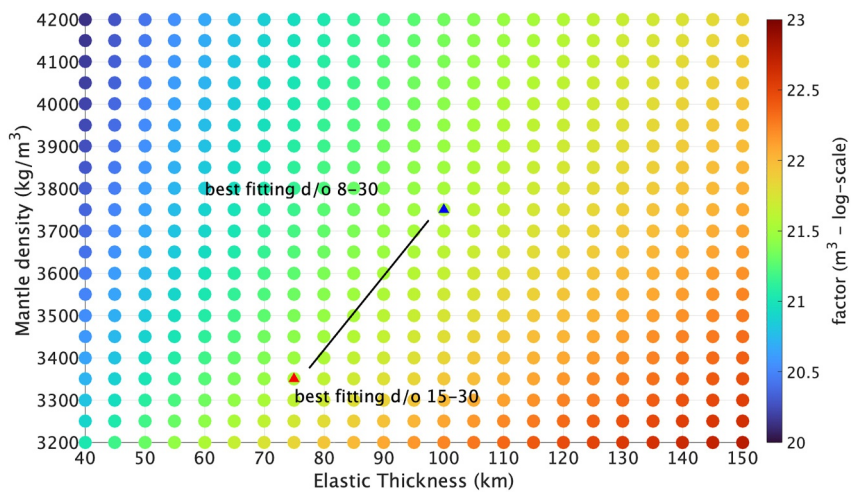

Figure 8. The elastic-rigidity-buoyancy factor from Equation 9 varied for the T_e and ρ_m parameters in the flexure modeling. Good fitting models are obtained for F_{flex} between 3.1623 and 3.981 10^{21} m^3 (black line), where best fits depend on the spectral bandwidth of the gravity field. The best fit model when using the spectral bandwidth degree and order 8–30 is denoted with a blue triangle (T_e is 100 km and ρ_m is 3,750 kg/m^3). When using shorter wavelengths of the gravity field due to the misalignment from the large impact basins, the best fit model when using the spectral bandwidth degree and order 15–30 is denoted with a red triangle (T_e is 75 km and ρ_m is 3,350 kg/m^3).

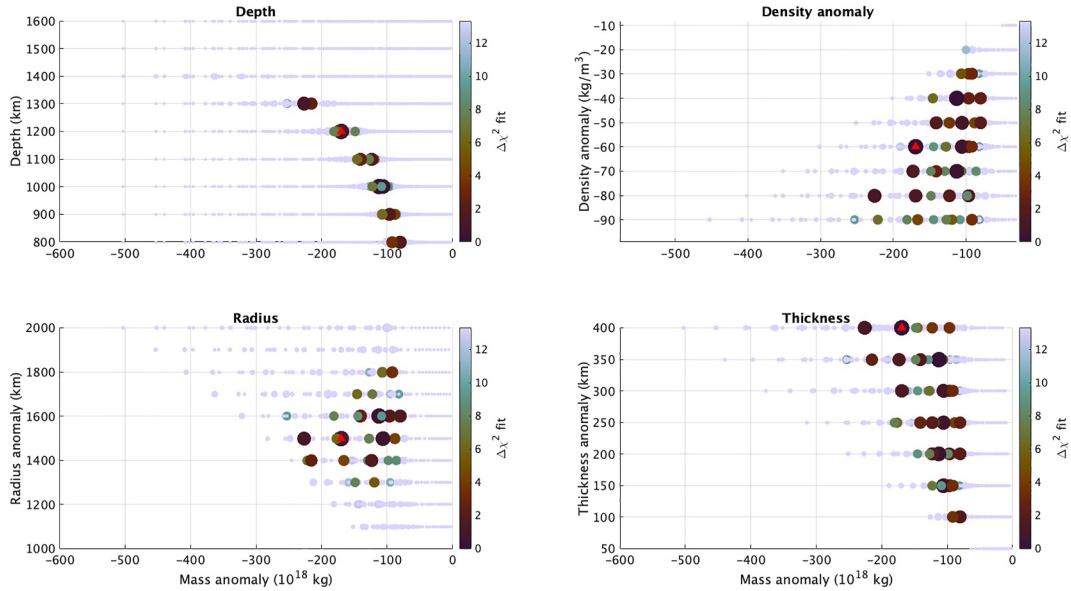

Figure 9. Full parameter search for the mass anomaly in the mantle underneath Tharsis Rise and its effect on the gravitational signal. The parameters are density anomaly of the disk with respect to the surrounding mantle, the radius of the disk, the thickness of the disk and the depth of the center of the disk. These values are shown with respect to the total mass anomaly of the mantle structure. The color scale and size of the marker show the Chi-square value in logarithmic scale of the degree variance of the SH coefficients between 2 and 8°. The best fitting model is shown with the red triangle.

the mantle: 100 km for elastic thickness and 3,750 kg/m^3 for the mantle density which are comparable to previous studies and have the preferred value for F_{flex} in the comparison with the observed gravity field.

4.2. Full Models With Deep Mass Anomaly

We will now analyze the model results obtained with the full modeling approach, using the flexure modeling together with the mantle convection code to compute the effect of the deep mantle anomaly. The parameters for the lithosphere are assigned the values determined in the previous section. The four parameters that characterize the deep mantle anomaly are: the density contrast with the surrounding mantle, the depth, the radius, and thickness of the disk as shown in Figure 3. In comparison to the observed gravity field, we focus on the long-wavelength part of the gravity field. We calculate the χ-squared value of the degree variance of the SH coefficients between 2 and 8°. The Chi-square fitness value is defined as:

$$\Delta\chi^2 = \sum_{i=1}^{N} \left(\frac{o_i - m_i}{\sigma_i}\right)^2 - \chi^2_{bestfit} \tag{22}$$

The number of elements (N) depends on the spectral domain that is chosen, here $N = 7$ for d/o 2 to 8. The observed values (o_i) minus the modeled values (m_i) are divided by the formal uncertainties of the observed values (σ_i), retrieved from the gravity model. In Figure 9, models with equal significance (1σ: $\chi^2 = 4.6$, $p = 0.66$) have larger marker size. The color scale is capped for models further away to the best fit model than 3σ: $\chi^2 = 13.3$, $p = 0.99$. The $\Delta\chi^2$ fitness value is shown with respect to the four mantle anomaly parameters are represented in Figure 9.

The results show a complex fitting of the geometry and characteristics of the mantle density anomaly. However, its mass anomaly seems to be constrained between −80 and −250 10^{18} kg. A less negative mass anomaly performs worse, so this shows that a deep mass anomaly is present in the mantle of Mars, in order to explain the gravity field. For the preferred mass values the structure is located at depths between 1,300 and 800 km, but with best results obtained at 1,200 km. The radius of the disk is between 1,300 and 1,800 km. The density contrast and thickness of the structure are less well constrained, but needs to be between −30 and −100 kg/m^3. The thickness

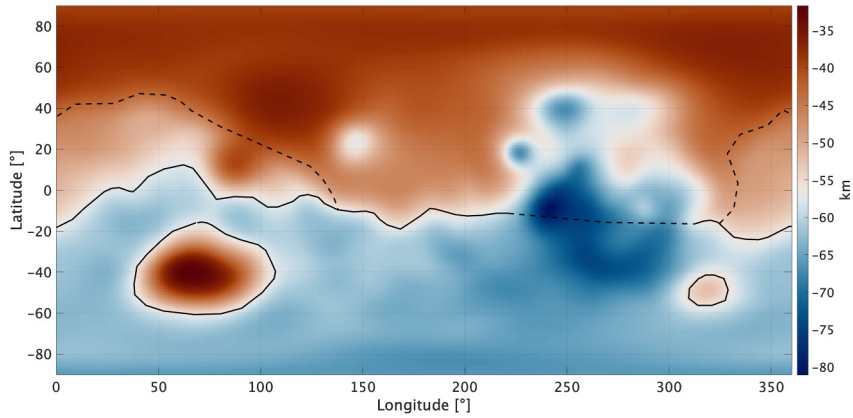

Figure 10. The resulting depth (with respect to 0 m topography) of the crust-mantle interface of the model. The clear dichotomy boundary in the crustal structure is indicated by the solid line. The Southern hemisphere shows two regions with thin crustal structure, produced by massive impacts: the Hellas and Argyre Basins. The dichotomy boundary at the Tharsis Rise is an estimate, with all late volcanism north of the line and limited to old volcanism only below the line. Other dashed lines could also be interpreted as dichotomy boundary.

of the disc is greater than 100 km, but realistic flatness estimates of the disc require the thickness of the structure to be less than 400 km. Figure S2 in Supporting Information S1 shows flatness estimates (R/t) values to be between 0.05 and 0.3.

The best fitting mass anomaly, meaning with the lowest chi-square value, is at a depth of 1,200 km, the radius of the disk is 1,500 km with a thickness of 400 km and the density anomaly with respect to the surrounding mantle is -60 kg/m^3. These values fall within the lower values of the Chi-square values presented in Figure 9. In Figure 4 the maximum positive dynamic topography is around 1.5 km and the negative topography, the ring around Tharsis, is about -0.5 km, with respect to the non-dynamic topography. The peak of Tharsis Rise, excluding the volcanoes, is around 7 km high, so around 20% of the topography is due to dynamic topography. This is similar to Zhong and Roberts (2003). The gravity residual with respect to our model (presented in Figure S1 in Supporting Information S1) has in total around 900 mGal variations (+639.0 mGal and -249.7 mGal), but the global signal around Tharsis Rise is no longer present in the residual signal (see Figure 12). Small-scale signals are visible that are related to regional density differences in the crust.

Figure 10 presents the resulting geometry of the crust-mantle interface of our lithosphere/mantle dynamic model. The crustal boundary shows a clear dichotomy with the Tharsis volcanoes on the dichotomy boundary. Compared

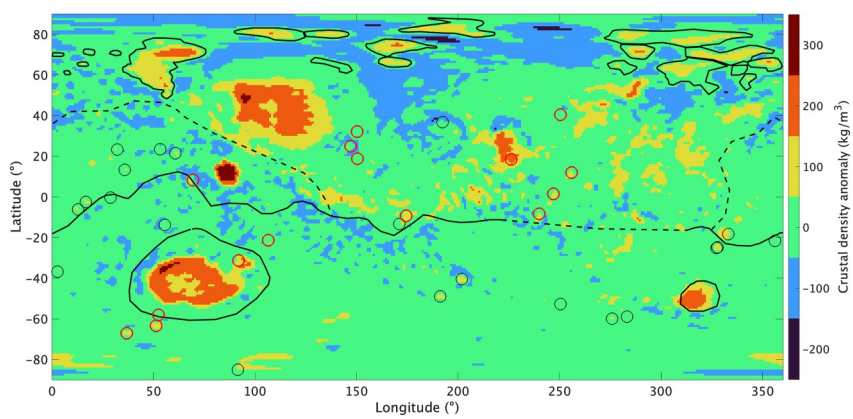

Figure 11. Crustal density variations with respect to the mean crustal density of 3,050 kg/m^3 from the flexure modeling. The dichotomy boundaries are plotted in black solid/dashed lines. The volcanoes are shown in red circles. Major impact craters of diameter larger than 300 km are shown in black circles. In the northern polar regions positive gravity anomalies are shown with black lines.

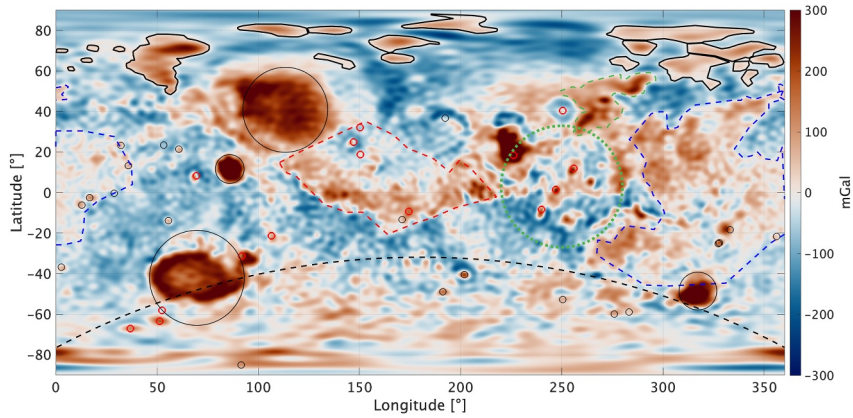

Figure 12. Gravity residual of our selected model. The size of the mantle plume with respect to the surface is shown in dotted green lines. Other anomalous mass regions are: Tempe Terra (dashed green), Elysium High Mass Lens (dashed red), High Mass Midlands (dashed blue), South Polar Area (dashed black), North Polar High Mass anomalies (solid black). Shield volcanoes are depicted by red circles. Large impact craters (>240 km) and basins are shown with black circles. The residual color map is saturated to ±300 mGal to enhance the small gravity features. Positive gravity anomalies go up to 666.7 mGal at Isidis Basin.

to other crustal models (Goossens et al., 2017; Neumann et al., 2004; Wieczorek & Zuber, 2004; Zuber et al., 2000), the crust-mantle interface underneath the northern part of the Tharsis Rise (−50 km) is similar. The southern hemisphere (−75 km) appears to be slightly deeper than the estimates from (Neumann et al., 2004; Zuber et al., 2000). With the newer crustal model from Wieczorek et al. (2022), we see that our crustal boundary resembles Wieczorek et al. (2022) large scale crustal thickness. They also predict a shallower crustal thickness in Arabia Terra, than the rest of the southern hemisphere. And similar variations crustal thickness patterns are seen in the Tharsis region. The thickest crust for both models are located underneath Arsia Mons.

The crustal thickness models of Wieczorek et al. (2022) predict the thinnest crust to be located in the Isidis Basin. The crust-mantle interface depth in Figure 11 shows that Hellas basin is the most shallow region. This, plus the fact that the lowest topography is at Hellas basin, results in the fact that our models tend to have the thinnest crust in Hellas Basin. Isidis Basin is much smaller and would therefore experience the rigidity of the thin shell much more, and would have a smaller crust-mantle anomaly, experiencing relatively thicker crust. The crustal thickness only depends on the topography of Mars in our approach. Wieczorek et al. (2022) compute their crust-mantle interface to solely be consistent with the observed gravitational field of the planet after correcting for the topographic, polar cap, and manual added lateral density variations. This explains why they estimate that Isidis Basin has the smallest crustal thickness. In our second step, we compute crustal structure with the residual gravity signal (everything our thin shell model cannot explain, gravitationally speaking) and we see the largest gravity residual at Isidis Basin. We interpret that as 75% intrusive mantle material. But Wieczorek et al. (2022) interpret that as crust-mantle interface changes, resulting in the thinnest crust at Isidis Basin. In all likelihood, a combination of both interpretations is very probably, and more regional studies of the crustal structure of Isidis Basin are needed to confirm this.

Underneath the huge volcanoes, the crust locally has large thickness values, but these are more spread out compared to previous models. The upward flow of the mantle plume is an extra force holding up the Tharsis Rise, negating the need for extra buoyancy and therefore sharp crustal thickness fluctuations. Hellas basin is the region with the shallowest crust-mantle interface (−30 km). Compensation of the deep basin is needed to explain the observed gravity signal, but from Figure 12 the crust-mantle interface should be even more shallow. The average crustal thickness estimate could be reduced as it is now larger than the InSight seismological data predicts (Knapmeyer-Endrun et al., 2021). However, reducing it to the thin values from Knapmeyer-Endrun et al. (2021) would create a negative crustal thickness in the Hellas Basin region and increase the mismatch of the data between the models and the gravity field observations. In conclusion, there still remains a mismatch between the seismological-derived and our gravity-based average crustal thickness estimates.

The crustal dichotomy, the difference in thickness between the northern and southern hemisphere, boundary of Neumann et al. (2004) is placed north of the Tharsis Rise, following the topographical zero height line. Zuber et al. (2000) introduced a boundary located further south, especially in the western part of the Tharsis Rise. Our model, shown in Figure 10, favors a crustal thickness that is much thinner underneath the northern part of the Tharsis Rise, as this can be explained by the dynamic topography of the deep mantle anomaly. The disconnection with the Tharsis Rise topography indicates that the dichotomy was present before the dome and is independent to the volcanic region. It is more in line with the dichotomy boundary by J. C. Andrews-Hanna et al. (2008), where the dichotomy boundary also crosses the Tharsis Region. An explanation could be that the older Martian dichotomy settled into isostatic equilibrium when the crust/lithosphere was still young and less rigid, supporting the top loads purely by buoyancy forces. When the lithosphere became older, it cooled down, and therefore increased both in thickness and rigidity, but freezing the local compensation of the dichotomy. This particular process can also explain the local compensation (McGovern et al., 2002; McGovern, Solomon, & Smith, 2004) of Hellas Basin, Argyre Basin, and probably the buried impact crater underneath Utopia Basin (Searls et al., 2006). Moreover, it seems to also explain the complex faults and graben systems covering the Tharsis Region and its surrounding (Banerdt et al., 1982). The cooling down and increasing rigidity of the lithosphere has resulted in the complex crustal structure that is seen today.

4.3. Crustal Density Inversion Using Residuals From the Our Global Model

Our model produces a gravity residual that shows no geologically correlated long-wavelength signal around the Tharsis Rise anymore. The residual map in Figure 12 shows gravity residuals that cannot be interpreted by a flexural lithosphere model and large deep mantle anomalies. These could be seen as sub-lithospheric mass anomalies, but due to the short-wavelength appearance it seems they are more related to crustal structures. For example, heavy basaltic crustal deposits in the Tharsis Region due to apparent volcanism compared to aeolian sandy deposits could result in several 100s kg/m^3 differences between the two regions.

Figure 12 shows the residuals of our best fitting model. There are several distinct regions and objects identified in this map. The Southern Hemisphere seems to contain overall higher mass anomalies than in the Northern Hemisphere, but the Northern Polar plains contain several local High Mass anomalies (NPHM). Several large impact basins are characterized with positive gravity anomalies: Hellas, Utopia, Isidis, and Argyre Basin. With the strongest residuals found at Isidis Basin. Most of the larger impact craters (>300 km diameter, depicted by black circles) seem to show a local increase in mass signature. Other localized high mass features are seen at locations of major shield volcanoes, depicted in red circles. Only Alba Mons and Peneus Patera seem to have limited positive mass signature. A lot of varying mass structures can be seen in the Tharsis region, showing young and maybe active geological restructuring of the crust. Most prominent are Olympus Mons, The Tharsis Volcanoes, and Tempe Terra, which are seen as high mass regions. Lower mass regions are Alba Mons and Acheron Fossae, and the southern region of the Tharsis Rise. Two other high mass features stand out, namely the Elysium High Mass Lens (EHML) and the High Mass Midlands (HMM) centered between Tharsis, Argyre Basin, Terra Sabaea, and Acidalia Planitia.

Figure 11 shows the crustal variations from the residual inversion from our flexure model. The density variations are plotted with respect to the mean density of 3,050 kg/m^3. Most of the density estimates fall within ±200 kg/m^3 variations, except for the large impact basins, which can go up to 300 kg/m^3. Furthermore, the northern plains overall seem to contain lighter crustal rocks, except for small regional areas with high density because of the positive residual gravity anomalies in those regions. The Tharsis Region contains slightly heavier crustal rocks, reflecting the basaltic outflows of the several volcanoes in the region.

5. Discussion

The InSight mission has provided the scientific community with a better constrained view of the interior of Mars, which proved essential to carry out a reanalysis of combined flexural and deep mantle dynamic study. Especially the reduction in crustal thickness values has helped a lot, as it allowed us to get the crustal thickness parameter out of the procedure. Our flexure experiment shows, as many other studies (McGovern, Solomon, et al., 2004; McKenzie et al., 2002; Belleguic et al., 2005; Beuthe et al., 2012; Broquet & Wieczorek, 2019), that the observed Martian gravity field cannot be represented by a flexure lithosphere model alone. We were able to better capture the long-wavelength spectral content by combining flexural models and dynamic mantle estimates. Thin shell

flexural models show significant improvement in the long-wavelengths of the gravity field, but fail to fully describe the pattern of the long-wavelength region between degree 2 and 8. The crustal thickness has always been a limiting parameter in the flexural studies, making the models ambiguous in selecting the average crustal thickness parameters. Our modeling took the range from Knapmeyer-Endrun et al. (2021) of 24–72 km as input but found that values below 45 km were not realistic, creating a negative crust in the Hellas Basin but reasonable values for the other parameters. Therefore, we worked with a value of 55 km, which is in between the seismic crustal thickness. Sensitivity analysis showed that an uncertainty of ±10 km did not significantly affect our conclusions. All of our models align with the crustal thickness estimate at the InSight location within the lower bound of 31 km and an upper bound of 47 km (Knapmeyer-Endrun et al., 2021). The value of the crustal thickness at the InSight location is 46.2 km for our model. This value is slightly higher compared to the estimate of 39 ± 8 km of Knapmeyer-Endrun et al. (2021), but falls within the estimates of crustal thickness of Kim et al. (2023).

5.1. Flexure Model of Mars

The spectral sensitivity helps in decoupling the flexural parameters. McKenzie et al. (2002) showed that the short wavelengths are suitable for determining the average crustal density, as we also found in our sensitivity study. Moreover, their crustal density of 2990 kg/m^3 is close to our estimate, supporting the idea that the average crustal density of Mars is higher than that on Earth. The crustal density in Goossens et al. (2017) is much lower but is based on gravity data starting from d/o 50 and higher. We show that only below degree 30 the sensitivity of the crustal density to the gravity data overlaps with the mantle density, crustal thickness, and elastic thickness. This means that d/o 30–50 can also be used to determine the crustal density. This changes the sensitivity of the gravity data used in Goossens et al. (2017) and can explain the higher estimate of the crustal density. When we look at studies that use a broad spectral domain we see the crustal density estimate is more related to our estimate (Wieczorek et al., 2022).

Other studies also use the mid wavelengths to estimate the Moho density contrast (or mantle density, when crustal density is already set) and the elastic thickness. McKenzie et al. (2002) modeled line-of-sight MGS data above the Tharsis bulge, estimating the elastic thickness to be 70 km for Tharsis, with a crustal density contrast of around 500 kg/m^3 for a top loading model. Other regional studies tend to keep the elastic thickness values roughly between 50 and 110 km with some exceptions. From admittance observations McGovern et al. (2002) found that most Martian volcanoes have $T_e = 20 - 160$ km (Olympus Mons larger than 140 km), several of the Chasma are above 120 km, but Hellas basin is mostly below 25 km (except southern rim 60–200 km), reflecting more local isostatic equilibrium in the lithosphere structure. Lowry and Zhong (2003) show a T_e of less than 200 km for Tharsis using bottom loading up to 420 km depth. However their crustal density estimate is quite low compared to our value, but they use a substantially larger crustal thickness that could explain this. Our flexure model show similar estimates, and can explain the ambiguity in the results, because the flexural-rigidity-buoyancy (F_{flex}) value is dependent on both T_e and ρ_m. The average mantle density of 3,750 kg/m^3 is on the high side, compared to upper mantle density estimates from Smrekar et al. (2019). The F_{flex} value shows that the topography and gravity have less sensitivity for the exact value of the mantle density, but that the combination of the parameters can be estimated. The high value could also be explained by the fact that the spherical harmonic degrees 8–30 of the gravity field, which are used to fit the mantle density, are sensitive to the lower mantle density and the deflections made by the pressure of the lithosphere.

More localized studies, like Belleguic et al. (2005), find that the densities of the Tharsis volcanoes seem to be about 3,200 ± 100 kg/m^3. This is in line with our findings, where we see that with an average crustal density of 3,050 kg/m^3 but most of the volcanoes need a slightly higher crustal density (100–200 kg/m^3) after the gravity residual inversion. The elastic thickness estimates of Belleguic et al. (2005) are 56 ± 20 km (Elysium Rise), 93 ± 40 km (Olympus Mons), 66 ± 20 (Alba Paterra), and 105 ± 40 km (Ascraeus Mons) for the Tharsis volcanoes. These values are slightly higher than the estimates of McGovern, Solomon, et al. (2004). A similar elastic thickness range was found by Beuthe et al. (2012) with values for Martian volcanoes above 80–110 km, except for Ascraeus Mons with $T_e = 20 - 60$ km. Grott and Wieczorek (2012) estimated the T_e of Tyrrhena Patera to be lower than 30 km using the admittance of degree 47–57. This low value could be attributed to the small spectral domain that was used and more sensitive to the local flexure structure. Figure 12 shows a substantial residual signal at this location, so volcanoes might have a lower local value for T_e. Independent modeling using tectonic

evidence of loading in the Tharsis region finds that the elastic thickness of the Tharsis Region is approximately 100 km to explain all the faulting (J. C. Andrews-Hanna et al., 2008). An extensive study re-evaluated the regional T_e values for different volcanoes and estimated T_e ranges of 0–100 km with uncertainties ranging from 200 km with and without bottom loading (Broquet & Wieczorek, 2019). Although most of these studies use regional analysis, our estimate T_e remains within their uncertainty limits, reflecting the fact that the average elastic thickness of Mars is between 75 and 100 km, depending on the actual mantle density. Our result for the rigidity of the lithosphere does conflict with local values for large impact basins. Hellas basin and Utopia basins seem to be best described with a low T_e value or even local isostasy in our modeling and previously found (McGovern et al., 2002). However, recent admittance studies (Deng et al., 2023) found larger and comparable T_e values to our global model. Nevertheless, it shows that the flexure model might not accurately capture all the physics involved of large impact basins on Mars or that a regional lower T_e estimate must be used, because of the reduced rigidity of the subsurface due to the impact.

5.2. Mantle Mass Anomaly

Hot mantle plumes could be the explanation for volcanic activity and local thinning of the lithosphere (Redmond & King, 2004). To explain late-to present-day melt Mars needs a substantial hot mantle and high activation energy of the mantle rock (Murphy & King, 2024). If confirmed, this would result in partial melting pockets in the mantle penetrating through the crust, which was seen to be difficult to reconcile with large elastic thickness estimates that suggest Mars is a cooled and sub-chondritic planet (Grott & Breuer, 2010). Our results show that it is plausible that a dynamic signature is needed to explain the topographic and gravity signature of the Tharsis Region.

If a thick elastic lithosphere of more than 150 km is considered, as proposed by flexure studies (McGovern et al., 2002; Zuber et al., 2000), a plume structure only had to account for a small part of the observed geoid (Phillips et al., 2001). Zhong and hong (2002) argued that the dynamical effects of mantle flow was over-predicted by earlier modeling, because of the omission of an elastic lithosphere constraining the mantle shell. Later modeling finds slightly stronger contributions of the mantle plume to the geoid (15%) and topography (25%) when a smaller elastic thickness is used (Zhong & Roberts, 2003). All these studies place the plume in the most shallow part of the upper mantle. Moreover, a thick lithosphere and crust might not be able to produce the magma volume required from the recent geological past observed on the surface of Mars (Kiefer, 2003). More realistic heating from the core can produce enough buoyant material to generate a plume that would cause enough melt beneath the surface that explains recent and historical lava flows (Li & Kiefer, 2007). By combining the dynamical plume model with a volcanic-constructed lithosphere, Redmond and King (2004) showed that both can and need to be taken into account to correctly reproduce the gravity, topography, and a source for melt to explain the recent lava flows.

Our study suggests that there is a light mass structure in the mantle underneath the Tharsis Rise, responsible for a significant part (ranging between $15 - 20$ percent) of the topographic uplift and gravity signal observed. We subtract dynamical topography from the observed topography first, before it is used in the flexure model. If the uncorrected topography is used for the flexure modeling only, any dynamic topography would leak into the modeled crustal structure. Linking residual topography then to dynamic models would underestimated the effect of mantle flow. The high topography at the Tharsis Region would otherwise always result in a thick lithosphere explaining the large gravity field, and there would not be any need to have dynamic topography. However, using also the information of the negative ring around Tharsis (fitting the complete spectrum) shows the need for a deep mantle anomaly. The resulting anomaly typically has a flatness ratio of 0.2 in our modeling, which could also be interpreted for the mantle plume heads (Ratcliff et al., 1998). This could suggests that a plume head is currently flowing upward toward the lithosphere to generate active volcanism in the geological future. Steinberger et al. (2010) suggested that there is a CMB structure, similar to the Large Low Seismic Velocity structures observed on Earth (Torsvik et al., 2008). Our flexure-only model structures cannot correctly produce the observed gravitational and topographic long-wavelength signature. A dynamic plume head seems therefore more plausible.

Other interpretations of the deep mantle mass anomaly could be the lithosphere as bottom loading, but Figure 9 shows a reduction in gravity fit for shallow anomalies. This is mostly due to the negative gravity ring around the Tharsis. For lithospheric or shallow sub-lithospheric mass anomalies it is more difficult to reproduce this feature. Recently, Huang et al. (2022) showed a seismic discontinuity at $1{,}006 \pm 40$ km by modeling the triplicated waveforms. The transition of olivine to wadsleyite not only induces a discontinuity in seismic velocities, but also

generates a density contrast. With a slightly higher adiabatic thermal profile underneath Tharsis this density contrast would happen at a lower depth generating a region with a thin negative density anomaly with respect to the average thermal state of Mars. This increase in thermal profile could be a hint to an ongoing plume or large local upwelling, also explaining the dynamic topography partly supporting the Tharsis Region.

Stable plumes are difficult to form in the current known mantle conditions, but seem possible to still exist (Plesa et al., 2018). For example, a lower magnesium number of the primitive mantle rock forming Mars causes the solidus to be 30–40° lower, enhancing the plume generation by 2–3 times (Kiefer et al., 2015). In addition, the abundance of water decreases the solidus, stimulating more plume activity in the Martian mantle (Kiefer & Li, 2016). These plumes will be responsible for large heat-flux values at the surface, but are difficult to observe since the crustal signature continues to dominate (Plesa et al., 2016). Unfortunately, the heat flow experiment onboard InSight did not go nominally, denying the validation of heat-flux model estimates reconciling plumes in the Martian mantle. Future missions should plan for more of these experiments also in the Tharsis Region. The current possibility of a mantle plume underneath the Elysium region, adjacent to the Utopia Planitia (Broquet & Andrews-Hanna, 2023) could suggest a more pronounced mantle plume activity in the current state of Mars. Our results show some residual signal south of the Elysium region but due to its smaller scale feature and proximity to the dichotomy boundary it is difficult to interpret.

The rather high density difference of the plume disk (-60 kg/m^3) could result in too high upward velocities (Steinberger & Antretter, 2006). However, the density of the disk is coupled with the size of the disk, so slightly increasing the disk size can reduce the density to lower values. The upward velocities for this mantle plume would be about tens to several cm/y, depending on the viscosity structure of the mantle. The consequence of allowing such a velocity is that the plume could travel the whole mantle from CMB to lithosphere in approximate 10–100 million years. A preference for an active plume head that flows upward can also be linked to the periodicity of volcanism observed in the geological record on Mars (Carr & Head, 2010). The first-order calculated rise time has a similar order size as the determined periodicity of volcanism on Mars. Recent volcanism, which can be linked to shergottites (Neukum et al., 2004), needs substantial melt that could suggest an active plume beneath the Tharsis Rise in the recent past. Localized high radiogenic heating (Schumacher & Breuer, 2006) could also explain the recent magmatism. If a plume is currently located at about the depth of the mid mantle, it is expected to have a new volcanism in the near geologic future. Therefore, new measurements are needed to determine whether the recent magmatism has a deep dynamic origin or whether it is related to shallower processes. A dynamic origin would imply more seismicity in the region, a change in long wavelength gravity field, and variations in the rotation rate of the planet. Recent observation of the Mars rotation rate (Le Maistre et al., 2023) could explain our estimates of a negative mass anomaly (-50 to -250 10^{18} kg) rising upward. The change of internal density would affect the moment of inertia of the planet and that would affect the rotation of the planet. The rotation has been increasing since the Viking observations such that the Martian day length decreased by 7.6×10^{-4} ms/yr, which can be linked to an upward rising negative mass anomaly in the mantle. We show in the Supporting Information S1 that this rotation rate acceleration in first order could be explained by our estimated mass anomaly. More precise analysis is needed to take into account the huge uncertainty in flow velocity in the mantle of Mars.

A major uncertainty in dynamic mantle flow studies is the viscosity structure of the mantle (Plesa et al., 2018; Samuel et al., 2021; Steinberger et al., 2010). In this study, we have used a 4 layer constant viscosity structure to reduce the unknown variables in the modeling, but the viscosity structure of Mars needs to be better constrained as it can drastically change the outcome of the geodynamic modeling. Preliminary studies (Thieulot et al., 2023) show that the variation of current viscosity models estimated from seismic data can almost remove or substantially increase the effect of dynamic topography generated by a plume body. From InSight data, a basal melt layer on top of the core was hypothesized (Khan et al., 2023; Samuel et al., 2021), which could have extra implications of the mantle flow and source of plume formation regions. In our modeling, we have chosen to neglect this hypothesis, but did introduced a free-slip boundary condition at the bottom of the mantle. This basal layer would have a reduced gravity effect, because the density contrast would be much smaller. The gravity effects due to the CMB deflections in our models are already small, so we expect that the basal layer will not have a drastic impact on our conclusions. We do suggest more modeling is needed to confirm this and more viscosity structures need to be explored. In order to truly find out whether there is an active plume underneath the Tharsis region, a dedicated satellite mission need to be sent to Mars to capture the gravity change. If a plume is moving, the time evolution of this mass anomaly due to its shear size could be captured by a sensitive gravity mission. The gravitational signal

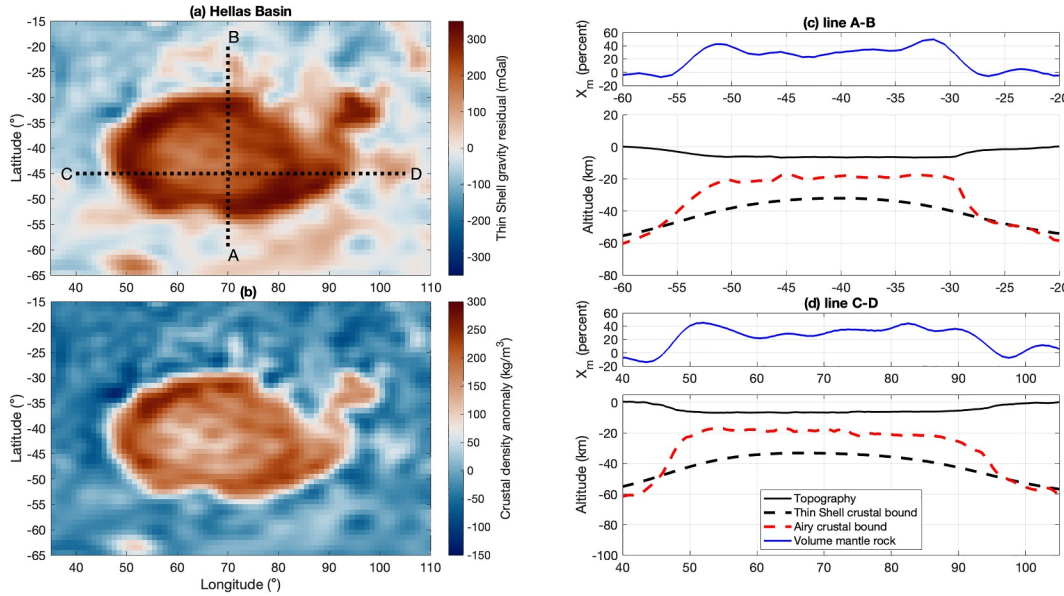

Figure 13. (a) Residual gravity anomalies for the Hellas Basin region. (b) The inverted crustal densities from the residual gravity anomalies. (c) Cross section A–B showing the volume percentage of mantle rock in the crust (blue). The topography (solid black), the geometry of the crust mantle interface from the thin shell model (dashed black) and the Airy model (dashed red). Horizontal axis represents the latitude of the cross section (d) similar to c, but for cross section C–D. Horizontal axis depicts the longitude of the cross section.

could already be present in several decades of satellite tracking data of missions such as MRO, MGS, and Mars Odyssey. A new mission proposal has been proposed (Wörner et al., 2023) in which a Satellite to Satellite Tracking type of mission is proposed using Quantum sensors for the laser link between the two spacecraft. This would result in very precise gravity data over several years and would be able to detect the changing mantle plume. Verification of an active mantle plume in Mars would have a huge impact on understanding the evolution of terrestrial planets. Moreover, it would results in better gravity and geodetic constraints for the polar caps mass changes (Wagner et al., 2024) and its Glacial Isostatic Adjustment effects to better constrain the interior viscosity structure of Mars (Broquet, Plesa, et al., 2025).

5.3. Residual Interpretation for 3D Crustal Structure

The residual anomalies presented in Figure 12 are mainly correlated with known topographic and geologic regions. Most prominent in the gravity residual are the large impact basins, Hellas and Utopia, with their high crustal density patterns. The modeling misfit of the gravitational effect of Hellas and Utopia basin by the thin shell model seems to affect the degree 4–10 spherical harmonic coefficients. Earlier study showed that these impact basins (McGovern et al., 2002; McGovern, Solomon, & Smith, 2004) are best modeled by a very low T_e or even with local isostasy ($T_e = 0$). Figures 13a and 13b show the gravity residual with the thin shell model. A significant gravity residual is seen in the middle of the basin. This corresponds to a positive crustal density that was computed by inverting this residual. The densities are 200–300 kg/m^3 higher crustal rocks than the surrounding regions. There is a sharp and clear boundary between the average- and high-density crust.

Figures 13c and 13d show a South-North and a West–East cross section of the Hellas basin. The geometry of the crustal bounds from the flexure model are compared to a fitting local isostasy model (Airy). Also, we plot the volumetric percentage of mantle rock in the crust that needs to be present to explain our inverted densities. The following formula computes this volumetric percentage (X_m) related to the mantle and crustal average densities and the density anomalies (seen in Figure 13b).

$$X_m = \frac{\Delta\rho}{\rho_m - \rho_c} \tag{23}$$

There is a clear correlation between the deviation of our model, the local isostatic model, and the volumetric mantle rock concentration. The average mantle rock percentage is 35 ± 5 percent. We performed similar computations for Utopia and Argyle basins (Figures S10 and S11 in Supporting Information S1) and found the same average mantle rock percentage in our crustal model. This could confirm the fact that Hellas, Utopia, and Argyle basin are locally compensated and are related to similar formation processes and conditions (age). Utopia basin is also thought to be linked to a major meteorite impact, then later buried by what seems more volcanic material and covered with a sedimentary layer from the northern ocean (Searls et al., 2006). Similar effects, however less pronounced, are assumed in the crustal structure of the Argyre basin, where crustal densities are estimated to be 200 kg/m^3 above average. Here, the basin is overprinted with a (aeolian) sedimentary layer, making the crustal anomaly interpretation more difficult. Therefore, higher-resolution gravity residuals could help to explore the geometry of the mantle rock in the crust.

Isidis basin has a more extreme value of 50 ± 25% of mantle rock in the crust (Figure S9 in Supporting Information S1). This high value, needed to describe the positive gravity anomaly in the area, suggests a larger igneous component than the other three basins. The residual gravity map in Figure 12 shows that Isidis basin has the largest gravity residual for the whole planet. As with Hellas and Utopia basin, some isostatic or even uncompensated crustal structure might be present in the current Martian crust. However, it seems that more extreme dynamics have played a role in the formation of Isidis, maybe even a secondary mantle upwelling. This is reflected in the crustal density map (Figure 11) by high density values up to more than 300–400 kg/m^3 with respect to the average crustal density. This high density signal could be interpreted as recent large magmatic chambers, or a volcanically infilled basin (Wagner & James, 2025). More regional modeling of these areas will provide insight into different crust-mantle interfaces or hidden magmatic regions underneath the basins. Ghent et al. (2012) and Ivanov et al. (2012) predicted magma flow fields and identified the eruption points. This correlates with the location of the largest residual gravity signal in that area, corroborating the magma chamber hypothesis.

The two large high mass regions, EHML and the HMM, are not visibly present in the density map. This indicates that those high-mass regions are due to the thinning of the crust. Despite the fact that they are separated by the young terrain of Tharsis region, it could be envisioned that these two blocks were linked in earlier geologic time and were created in a similar event. The Elysium volcanic fields might be much younger and have not yet a sufficiently strong mass signature to make the two geologic blocks seem different from the standpoint of gravitation modeling. South of the EHML we see a negative density region. This area resembles the high concentrations of thorium found in Bouley et al. (2020). It does not cover the entire Cimmeria-Sirenum crustal block, but only the regions with high potassium and thorium concentrations of that block. The negative density could be due to the higher thermal flux in the crust, making the rock material slightly less heavy. This could explain the lighter crustal density in the southern highlands.

As was already observed in the gravity residual plot (Figure 12), almost all major shield volcanoes are related to a high mass anomaly centered at the crater mount. This high mass is also transformed into a high density estimate of 100 kg/m^3 higher than surrounding terrain in most cases or even 200 kg/m^3 in the case of Olympus Mons. This high density could be related to intrusive magma into the crust which results in overall higher crustal density at those locations. The Northwest flanks of Olympus Mons show further increased density of the crustal material. This is related to the large collapse and flow fields of the west flank, which compact and deposit heavy basaltic material (McGovern, Smith, et al., 2004). Two volcanoes show a reduced version of this typical high-density signal: Alba Mons and Peneus Patera. Alba Mons is situated in a less dense region, which makes the high-mass intrusive magma less visible as is seen in Figure 12. Moreover, Alba Mons is quite shallow but has a large diameter. This could also explain why the intrusive magma is less visible in the data as a substantial high density value. The amount of intrusive magma is more spread out over a larger area, therefore reducing the bulk crustal density compared to volcanoes with a much smaller diameter. More regional and precise data is needed to map the intrusive magma for Alba Mons. Peneus Patera is located on the rim of the Hellas Basin. This major event has compacted the surrounding crustal structure so much that the high density of the intrusive magma does not have a high contrast with the surrounding crustal structure to be visible. Only one shield volcano has a different gravitational signature and that is one of the Elysium volcanoes, Hecates Tholus. We see in this case a negative gravity anomaly surrounded with positive crustal gravity signature. It is unclear why this reversed feature is seen, which could be related to its small size or a collapsed magma chamber, resulting in a void space in the volcano.

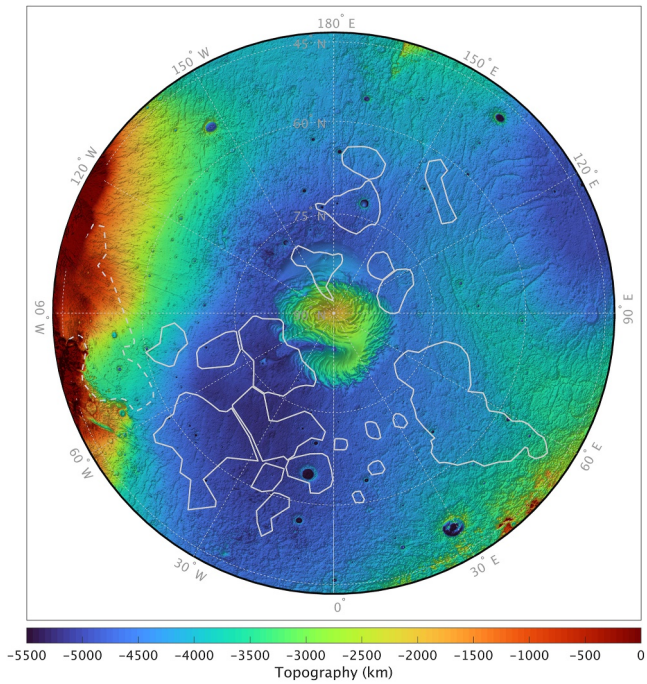

Figure 14. Northern Polar plains showing the North Polar High Mass (NPHM) structures on the topographic map of the region. The NPHM (solid gray line) are all located in the Borealis Basin and they seem to be mostly concentrated in the Borealis back-arc Basin and The Acidalia Basin. The gray dashed line on the left is depicting the high mass Tempe Terra Region.

Comparing the densities of these volcanoes with the estimates of Broquet and Wieczorek (2019), we see that they are similar to the density values of the $L = 0$ models, or non-bottom loading models. Our local density estimates seem to fall within, or overlap with their uncertainty estimates with the exception of for Elysium Mons, where we estimate a density of 3,050 kg/m^3, but Broquet and Wieczorek (2019) arrive at larger densities (3,320 ± 20 kg/m^3) for their non-loaded models, and even higher for the loaded models. Other strongly correlated positive gravity signatures are large impact basins (>300 km diameter). Of the 21 large impact craters, 75% of them show a positive gravity residual of 50–250 mGal. This surplus mass could be related to impact-induced excavation of the crust and mantle uplift. It could also be explained by compaction of the crustal rock by the impact or some sort of limited magma intrusion caused by the event. This could be seen as a similar process, but on a smaller scale, as with large impact basins, like the Hellas and Isidis Basin, and mascons on the Moon (Zhao et al., 2021). More regional research is needed to understand the relation of this high mass signal compared to the size of the impact crater. A very recent study suggests a re-analysis of the volcanic intrusive to extrusive magma deposition determined by gravity and topography studies (Wagner & James, 2025). Our iterative approach (Figure S5 in Supporting Information S1) described in the Supporting Information S1 shows limited effect to the crustal density (<2 kg/m^3), which could be interpreted as intrusive magmatism.

The polar regions show no correlation between the gravity residual and the geometry of the polar ice caps. The models by Khuller and Plaut (2021b) and Nerozzi et al. (2022) seem to capture the gravitational attraction of the ice caps well enough. In the northern planes, some interesting positive gravity anomalies arise (NPHM), not correlated to the ice cap, the largest of which is located 60° east and 70° north of the boundary between Utopia and Acidalia Planitia and Planum Boreum. This was also seen in the density perturbations predicted in the first 50 km by Arkani-Hamed and Riendler (2002). However, more positive anomalies are scattered around (also in Arcadia Planitia) the northern region of Mars. These anomalies do not have a strong topographical component and therefore cannot be explained by the flexure model or isostatic uplift.

Figure 14 shows the contours of these anomalies with respect to the topography of the northern hemisphere. All buried mass structures seem to be located in the Borealis basin (Buczkowski, 2007). Two concentrations are seen in the Acidalia basin and the back arc Borealis basin. Most of the subsurface mass structures can be found there. The thick sedimentary cover could explain why they do not have any topographic signature. The largest North Polar High Mass (NPHM) anomaly is on the border of the Borealis basin and is partly overlaying Terra Arabia. This area is the boundary between the Utopia and Borealis basins. Smaller mass features are seen and could be structurally altered crustal blocks due to the large impact that made Utopia. The large NPHM anomaly also seems to be composed of several crustal structures, with the highest mass located in the Borealis basin. Tempe Terra shows similar positive density/gravity signatures. Its proximity to some of the NPHM anomalies in the Acidalia basin could suggest a similar nature, but further geological research is needed to confirm this. The round character of some of the NPHM anomalies can indicate buried craters as well. Several smaller anomalies are seen in the northern planes, but the resolution of the gravity data makes it difficult to identify them as such. The northern hemisphere has many buried impact craters, named Quasi-Circular Depressions (QCDs), that are indications of an Early Noachian age, maybe going back to the primordial crust, now overprinted by southern erosion deposits (Buczkowski et al., 2005; Frey et al., 2002). This explains the partial overprinting by the Tharsis Rise of the northern hemisphere. When the QCDs are interpreted as impact craters and taken into account in the determination of the age by crater counting, the northern basement underneath the sedimentary layers seem to be older (Frey, 2006; Frey et al., 2002) than the southern highlands. This supports an evolutionary model that suggests the southern highlands were created by a huge basaltic deposit (Roberts & Zhong, 2007), compared to the huge impact theory (Ballantyne et al., 2023). It is therefore important to verify and analyze the nature of these QCDs more, with techniques that could also study the subsurface structure of the identified regions of Frey et al. (2002).

Most large surface impact craters show a high mass anomaly centered with the impact crater. A detailed study of the gravity signature for these types of impact craters is needed while taking into account that these craters are later covered by oceanic sediments, reflecting the geologic environment of the northern hemisphere of Mars.

Finally, other geological areas of Mars stand out. Archeon Fossea seems to be relatively lighter than the surrounding crustal rocks. This old feature could be having large tectonic restructuring, due to the adjacent Olympus Mons, fracturing the rock and introducing many crack and void that would lower the averaged density of that structure. The surface of Archeon Fossae is highly fractured and shows many valleys. Furthermore, Valles Marineris is modeled well as the low wavelength scale of that feature is captured by uncompensated model response. It does not seem to be related to a major density contrast of the crustal structure. Moreover, the large but relatively thin canyons have little to no effect on the crust-mantle interface in that region, suggesting a shallow cause of the creation of this canyon. This corroborates the idea the Valles Marineris was created by substantial igneous intrusions responsible for the removal of ice, carbonates or magma (J. C. Andrews-Hanna, 2012a; J. C. Andrews-Hanna, 2012b, 2012c) or a huge dike insertion creating the topography signature of the Valley (Özeren et al., 2014).

6. Conclusion

The InSight mission to Mars has provided the community with new observations that can be used to better understand the interior of Mars. This new information made it possible to better constrain the properties of the lithosphere and mantle dynamics of the Martian interior. Our study shows that the presence of a substantial negative mass anomaly deep in the mantle underneath the Tharsis region is a plausible explanation for the observed long-wavelength gravity field and topography. The best fitting mass anomaly has the following dimensions: the radius is 1,500 km, the thickness is 400 km, the density anomaly of -60 kg/m^3, and at a depth of 1,200 km. The geometry of the anomaly could be interpreted as a huge plume head that is traveling upwards, dynamically supporting the region. The resulting Martian lithosphere was modeled by a thin shell model. The Martian crust has a crustal thickness of 55 ± 10 km and an average density of 3,050 kg/m^3. The flexural rigidity and buoyancy effects can be modeled by mantle density ranging between 3,300 and 4,050 kg/m^3, and elastic thicknesses between 70 and 120 km. The preferred flexural-rigidity-buoyancy factor is between 3.1623 and 3.3981 10^{21} m^3.

The gravity residual between the observed and modeled gravity fields appears to be strongly correlated with Martian crustal geology. We identify several distinct high- and low-mass regions associated with specific geological provinces. Large impact basins appear to have higher densities than the average crustal rock, while the large shield volcanoes are also characterized by high-mass anomalies. The large impact basins Hellas and Utopia appear to be in isostatic equilibrium, suggesting an early formation. The Isidis basin shows strong gravitational evidence for magma chambers within the crust. Buried mass anomalies are detected in the northern polar plains by inspecting the residual gravity anomalies. The origin of these anomalies is unclear but seems to have two possible geological explanations: (a) they could represent structures similar to those in the Tempe Terra region, based on the similar gravity signatures and their proximity to Tempe Terra; or (b) they could correspond to large, ancient impact craters, similar to previously identified QCDs in MOLA data, suggesting an older geological history for the northern hemisphere of Mars than previously recognized.

Our lithosphere and mantle model of Mars introduces opportunities to study the planet's subsurface. Moreover, it suggests that the time is ripe for a dedicated gravity mission to Mars to follow up on the success of GRACE- and GRAIL-type missions and to further advance our understanding of the Martian interior.

Conflict of Interest

The authors declare no conflicts of interest relevant to this study.

Data Availability Statement

The GSH code is to be found and archived at 4TU.Research Root (2021). For SFEC and the Mars modeling scenario, the code is archived at 4TU.Research Tosi et al. (2024). With this code, all results can be reproduced. All the data used in this paper are described in Section 2. For the topography data we used the publicly available

MOLA data (Smith, Zuber, et al., 2003). The gravity data in this study is the JMRO-120d model (Konopliv et al., 2016). To correct for the ice sheet loading we used ice sheet thickness models for the North pole (Nerozzi et al., 2022) and the South pole (Khuller & Plaut, 2021a). Additional reference in the supplementary material are Comer et al. (1985), Kalousová et al. (2012), and Konopliv et al. (2011).

Acknowledgments
This paper would not have been possible without the InSight mission revealing the interior of Mars. We are grateful for the two reviewers and editor with their details comments on the previous versions of the manuscript and Sam Fayolle for proofreading. Furthermore, we thank all the people and institutes to make the data available to the public. We would like to mention Maxime Vincent for preliminary runs on benchmarking part of the modeling software.

References

Anderson, R. C., Dohm, J. M., Golombek, M. P., Haldemann, A. F. C., Franklin, B. J., Tanaka, K. L., et al. (2001). Primary centers and secondary concentrations of tectonic activity through time in the western hemisphere of Mars. *Journal of Geophysical Research*, *106*(E9), 20563–20585. https://doi.org/10.1029/2000JE001278

Andrews-Hanna, J., & Broquet, A. (2023). The history of global strain and geodynamics on mars. *Icarus*, *395*, 115476. https://doi.org/10.1016/j.icarus.2023.115476

Andrews-Hanna, J. C. (2012a). The formation of valles marineris: 1. tectonic architecture and the relative roles of extension and subsidence. *Journal of Geophysical Research*, *117*(E3), E03006. https://doi.org/10.1029/2011JE003953

Andrews-Hanna, J. C. (2012b). The formation of valles marineris: 2. stress focusing along the buried dichotomy boundary. *Journal of Geophysical Research*, *117*(E4), E04009. https://doi.org/10.1029/2011JE003954

Andrews-Hanna, J. C. (2012c). The formation of valles marineris: 3. trough formation through super-isostasy, stress, sedimentation, and subsidence. *Journal of Geophysical Research*, *117*(E6), E06002. https://doi.org/10.1029/2012JE004059

Andrews-Hanna, J. C., Zuber, M. T., & Hauck, S. A. (2008). Strike-slip faults on Mars: Observations and implications for global tectonics and geodynamics. *Journal of Geophysical Research*, *113*(E8), E08002. https://doi.org/10.1029/2007JE002980

Arkani-Hamed, J., & Riendler, L. (2002). Stress differences in the martian lithosphere: Constraints on the thermal state of mars. *Journal of Geophysical Research*, *107*(E12), 2-1–2-6. https://doi.org/10.1029/2002JE001851

Audet, P. (2014). Toward mapping the effective elastic thickness of planetary lithospheres from a spherical wavelet analysis of gravity and topography. *Physics of the Earth and Planetary Interiors*, *35*. https://doi.org/10.1016/j.pepi.2013.09.011

Ballantyne, H. A., Jutzi, M., Golabek, G. J., Mishra, L., Cheng, K. W., Rozel, A. B., & Tackley, P. J. (2023). Investigating the feasibility of an impact-induced martian dichotomy. *Icarus*, *392*, 115395. https://doi.org/10.1016/j.icarus.2022.115395

Banerdt, W. B., Golombek, M. P., & Tanaka, K. L. (1992). Stress and tectonics on Mars. In M. George (Ed.), *Mars* (pp. 249–297). NASA.

Banerdt, W. B., Phillips, R. J., Sleep, N. H., & Saunders, R. S. (1982). Thick shell tectonics on one-plate planets: Applications to mars. *Journal of Geophysical Research*, *87*(B12), 9723–9733. https://doi.org/10.1029/JB087iB12p09723

Banerdt, W. B., Smrekar, S. E., Banfield, D., Giardini, D., Golombek, M., Johnson, C. L., et al. (2020). Initial results from the InSight mission on Mars. *Nature Geoscience*, *13*(3), 183–189. https://doi.org/10.1038/s41561-020-0544-y

Belleguic, V., Lognonné, P., & Wieczorek, M. A. (2005). Constraints on the Martian lithosphere from gravity and topography data. *Journal of Geophysical Research*, *110*(E11), E11005. https://doi.org/10.1029/2005JE002437

Beuthe, M. (2008). Thin elastic shells with variable thickness for lithospheric flexure of one-plate planets. *Geophysical Journal International*, *172*(2), 817–841. https://doi.org/10.1111/j.1365-246X.2007.03671.x

Beuthe, M., Le Maistre, S., Rosenblatt, P., Pätzold, M., & Dehant, V. (2012). Density and lithospheric thickness of the Tharsis Province from MEX MaRS and MRO gravity data: Density and lithosphere of tharsis. *Journal of Geophysical Research*, *117*(E4). https://doi.org/10.1029/2011JE003976

Bouley, S., Baratoux, D., Matsuyama, I., Forget, F., Séjourné, A., Turbet, M., & Costard, F. (2016). Late tharsis formation and implications for early mars. *Nature*, *531*(7594), 344–347. https://doi.org/10.1038/nature17171

Bouley, S., Baratoux, D., Paulien, N., Missenard, Y., & Saint-Bã©zar, B. (2018). The revised tectonic history of tharsis. *Earth and Planetary Science Letters*, *488*, 126–133. https://doi.org/10.1016/j.epsl.2018.02.019

Bouley, S., Keane, J., Baratoux, D., Langlais, B., Matsuyama, I., Costard, F., et al. (2020). A thick crustal block revealed by reconstructions of early mars highlands. *Nature Geoscience*, *13*(2), 105–109. https://doi.org/10.1038/s41561-019-0512-6

Broquet, A., & Andrews-Hanna, J. C. (2023). Geophysical evidence for an active mantle plume underneath elysium planitia on mars. *Nature Astronomy*, *7*(2), 160–169. https://doi.org/10.1038/s41550-022-01836-3

Broquet, A., Maia, J., & Wieczorek, M. A. (2025). On the crustal architecture of the terrestrial planets. *Journal of Geophysical Research: Planets*, *130*(9), e2025JE009139. https://doi.org/10.1029/2025JE009139

Broquet, A., Plesa, A. C., Klemann, V., Root, B. C., Genova, A., Wieczorek, M. A., et al. (2025). Glacial isostatic adjustment reveals mars's interior viscosity structure. *Nature*, *639*(8053), 109–113. https://doi.org/10.1038/s41586-024-08565-9

Broquet, A., & Wieczorek, M. A. (2019). The gravitational signature of Martian volcanoes. *Journal of Geophysical Research: Planets*, *124*(8), 2054–2086. https://doi.org/10.1029/2019JE005959

Broquet, A., Wieczorek, M. A., & Fa, W. (2020). Flexure of the lithosphere beneath the north polar cap of mars: Implications for ice composition and heat flow. *Geophysical Research Letters*, *47*(5), e2019GL086746. https://doi.org/10.1029/2019GL086746

Broquet, A., Wieczorek, M. A., & Fa, W. (2021). The composition of the south polar cap of mars derived from orbital data. *Journal of Geophysical Research: Planets*, *126*(8), e2020JE006730. https://doi.org/10.1029/2020JE006730

Buczkowski, D. L. (2007). Stealth quasi-circular depressions (sqcds) in the northern lowlands of mars. *Journal of Geophysical Research*, *112*(E9), E09002. https://doi.org/10.1029/2006JE002836

Buczkowski, D. L., Frey, H. V., Roark, J. H., & McGill, G. E. (2005). Buried impact craters: A topographic analysis of quasi-circular depressions, utopia basin, mars. *Journal of Geophysical Research*, *110*(E3), E03007. https://doi.org/10.1029/2004JE002324

Carr, M. H., & Head, J. W. (2010). Geologic history of mars. *Earth and Planetary Science Letters*, *294*(3–4), 185–203. https://doi.org/10.1016/j.epsl.2009.06.042

Comer, R. P., Solomon, S. C., & Head, J. W. (1985). Mars: Thickness of the lithosphere from the tectonic response to volcanic loads. *Reviews of Geophysics*, *23*(1), 61–92. https://doi.org/10.1029/RG023i001p00061

Deng, Q., Zhong, Z., Ye, M., Zhang, W., Qiu, D., Zheng, C., et al. (2023). Lithospheric loading model for large impact basins where a mantle plug is present. *Journal of Geophysical Research: Planets*, *128*(6), e2022JE007620. https://doi.org/10.1029/2022JE007620

Ding, M., Lin, J., Gu, C., Huang, Q., & Zuber, M. T. (2019). Variations in martian lithospheric strength based on gravity/topography analysis. *Journal of Geophysical Research: Planets*, *124*(11), 3095–3118. https://doi.org/10.1029/2019JE005937

Frey, H. V. (2006). Impact constraints on, and a chronology for, major events in early mars history. *Journal of Geophysical Research*, *111*(E8), E08S91. https://doi.org/10.1029/2005JE002449

Frey, H. V., Roark, J. H., Shockey, K. M., Frey, E. L., & Sakimoto, S. E. H. (2002). Ancient lowlands on mars. *Geophysical Research Letters*, *29*(10), 22-1–22-4. https://doi.org/10.1029/2001GL013832

Genova, A., Goossens, S., Lemoine, F. G., Mazarico, E., Neumann, G. A., Smith, D. E., & Zuber, M. T. (2016). Seasonal and static gravity field of Mars from MGS, Mars Odyssey and MRO radio science. *Icarus*, *272*, 228–245. https://doi.org/10.1016/j.icarus.2016.02.050

Ghent, R. R., Anderson, S. W., & Pithawala, T. M. (2012). The formation of small cones in isidis planitia, mars through mobilization of pyroclastic surge deposits. *Icarus*, *217*(1), 169–183. https://doi.org/10.1016/j.icarus.2011.10.018

Golabek, G. J., Keller, T., Gerya, T. V., Zhu, G., Tackley, P. J., & Connolly, J. A. (2011). Origin of the martian dichotomy and tharsis from a giant impact causing massive magmatism. *Icarus*, *215*(1), 346–357. https://doi.org/10.1016/j.icarus.2011.06.012

Goossens, S., Sabaka, T. J., Genova, A., Mazarico, E., Nicholas, J. B., & Neumann, G. A. (2017). Evidence for a low bulk crustal density for Mars from gravity and topography: Low bulk crustal density for mars. *Geophysical Research Letters*, *44*(15), 7686–7694. https://doi.org/10.1002/2017GL074172

Grott, M., & Breuer, D. (2010). On the spatial variability of the martian elastic lithosphere thickness: Evidence for mantle plumes? *Journal of Geophysical Research*, *115*(E3), E03005. https://doi.org/10.1029/2009JE003456

Grott, M., & Wieczorek, M. (2012). Density and lithospheric structure at tyrrhena patera, mars, from gravity and topography data. *Icarus*, *221*(1), 43–52. https://doi.org/10.1016/j.icarus.2012.07.008

Hager, B. H., & O'Connell, R. J. (1981). A simple global model of plate dynamics and mantle convection. *Journal of Geophysical Research*, *86*(B6), 4843–4867. https://doi.org/10.1029/JB086iB06p04843

Harder, H. (1998). Phase transitions and the three-dimensional planform of thermal convection in the martian mantle. *Journal of Geophysical Research*, *103*(E7), 16775–16797. https://doi.org/10.1029/98JE01543

Harder, H., & Christensen, U. (1996). A one-plume model of martian mantle convection. *Nature*, *380*(6574), 507–509. https://doi.org/10.1038/380507a0

Hartmann, W. K., & Neukum, G. (2001). Cratering chronology and the evolution of mars. *Space Science Reviews*, *96*(1), 165–194. https://doi.org/10.1023/A:1011945222010

Hauber, E., Brož, P., Jagert, F., Jodłowski, P., & Platz, T. (2011). Very recent and wide-spread basaltic volcanism on mars. *Geophysical Research Letters*, *38*(10), L10201. https://doi.org/10.1029/2011GL047310

Hirt, C., Kuhn, M., Featherstone, W. E., & Göttl, F. (2012). Topographic/isostatic evaluation of new-generation goce gravity field models. *Journal of Geophysical Research*, *117*(B5), B05407. https://doi.org/10.1029/2011JB008878

Huang, Q., Schmerr, N. C., King, S. D., Kim, D., Rivoldini, A., Plesa, A.-C., et al. (2022). Seismic detection of a deep mantle discontinuity within mars by insight. *Proceedings of the National Academy of Sciences*, *119*(42), e2204474119. https://doi.org/10.1073/pnas.2204474119

Ivanov, M., Hiesinger, H., Erkeling, G., Hielscher, F., & Reiss, D. (2012). Major episodes of geologic history of isidis planitia on mars. *Icarus*, *218*(1), 24–46. https://doi.org/10.1016/j.icarus.2011.11.029

Kalousová, K., Souček, O., & Čadek, O. (2012). Deformation of an elastic shell with variable thickness: A comparison of different methods. *Geophysical Journal International*, *190*, 726–744. https://doi.org/10.1111/j.1365-246X.2012.05539.x

Khan, A., Ceylan, S., van Driel, M., Giardini, D., Lognonné, P., Samuel, H., et al. (2021). Upper mantle structure of Mars from InSight seismic data. *Science*, *373*(6553), 434–438. https://doi.org/10.1126/science.abf2966

Khan, A., Huang, D., Durán, C., Sossi, P. A., Giardini, D., & Murakami, M. (2023). Evidence for a liquid silicate layer atop the martian core. *Nature*, *622*(7984), 718–723. https://doi.org/10.1038/s41586-023-06586-4

Khuller, A., & Plaut, J. (2021a). Characteristics of the basal interface of the martian south polar layered deposits (Tech. Rep. No. Version 1) [Dataset]. *Zenodo*. https://doi.org/10.5281/zenodo.4653741

Khuller, A. R., & Plaut, J. J. (2021b). Characteristics of the basal interface of the martian south polar layered deposits. *Geophysical Research Letters*, *48*(13), e2021GL093631. https://doi.org/10.1029/2021GL093631

Kiefer, W. S. (2003). Melting in the martian mantle: Shergottite formation and implications for present-day mantle convection on mars. *Meteoritics & Planetary Sciences*, *38*(12), 1815–1832. https://doi.org/10.1111/j.1945-5100.2003.tb00017.x

Kiefer, W. S., Filiberto, J., Sandu, C., & Li, Q. (2015). The effects of mantle composition on the peridotite solidus: Implications for the magmatic history of Mars. *Geochimica et Cosmochimica*, *162*, 247–258. https://doi.org/10.1016/j.gca.2015.02.010

Kiefer, W. S., & Li, Q. (2016). Water undersaturated mantle plume volcanism on present-day mars. *Meteoritics & Planetary Sciences*, *51*(11), 1993–2010. https://doi.org/10.1111/maps.12720

Kim, D., Duran, C., Giardini, D., Plesa, A.-C., Stähler, S. C., Boehm, C., et al. (2023). Global crustal thickness revealed by surface waves orbiting mars. *Geophysical Research Letters*, *50*(12), e2023GL103482. https://doi.org/10.1029/2023GL103482

Kite, E. S., Matsuyama, I., Manga, M., Perron, J. T., & Mitrovica, J. X. (2009). True polar wander driven by late-stage volcanism and the distribution of paleopolar deposits on mars. *Earth and Planetary Science Letters*, *280*(1), 254–267. https://doi.org/10.1016/j.epsl.2009.01.040

Knapmeyer-Endrun, B., Panning, M. P., Bissig, F., Joshi, R., Khan, A., Kim, D., et al. (2021). Thickness and structure of the martian crust from InSight seismic data. *Science*, *373*(6553), 438–443. https://doi.org/10.1126/science.abf8966

Konopliv, A. S., Asmar, S. W., Folkner, W. M., Özgür, K., Nunes, D. C., Smrekar, S. E., et al. (2011). Mars high resolution gravity fields from mro, mars seasonal gravity, and other dynamical parameters. *Icarus*, *211*(1), 401–428. https://doi.org/10.1016/j.icarus.2010.10.004

Konopliv, A. S., Park, R. S., & Folkner, W. M. (2016). An improved jpl mars gravity field and orientation from mars orbiter and lander tracking data. *Icarus*, *274*, 253–260. https://doi.org/10.1016/j.icarus.2016.02.052

Kraus, H. (1967). *Thin elastic shells: An introduction to the theoretical foundations and the analysis of their static and dynamic behavior*. John Wiley and Sons.

Le Maistre, S., Rivoldini, A., Caldiero, A., Yseboodt, M., Baland, R.-M., Beuthe, M., et al. (2023). Spin state and deep interior structure of mars from insight radio tracking. *Nature*, *619*(7971), 733–737. https://doi.org/10.1038/s41586-023-06150-0

Li, Q., & Kiefer, W. S. (2007). Mantle convection and magma production on present-day mars: Effects of temperature-dependent rheology. *Geophysical Research Letters*, *34*(16), L16203. https://doi.org/10.1029/2007GL030544

Lowry, A. R., & Zhong, S. (2003). Surface versus internal loading of the tharsis rise, mars. *Journal of Geophysical Research*, *108*(E9), 5099. https://doi.org/10.1029/2003JE002111

Martinec, Z. (2014). Mass-density green's functions for the gravitational gradient tensor at different heights. *Geophysical Journal International*, *196*(3), 1455–1465. https://doi.org/10.1093/gji/ggt495

Matsuyama, I., & Manga, M. (2010). Mars without the equilibrium rotational figure, tharsis, and the remnant rotational figure. *Journal of Geophysical Research*, *115*(E12), E12020. https://doi.org/10.1029/2010JE003686

McGovern, P. J., Smith, J. R., Morgan, J. K., & Bulmer, M. H. (2004). Olympus mons aureole deposits: New evidence for a flank failure origin. *Journal of Geophysical Research*, *109*(E8), E08008. https://doi.org/10.1029/2004JE002258

McGovern, P. J., Solomon, S. C., & Smith, D. E. (2004). Correction to "Localized gravity/topography admittance and correlation spectra on Mars: Implica1414 tions for regional and global evolution". *Journal of Geophysical Research*, *109*(E7), E07007. https://doi.org/10.1029/2004JE002286

McGovern, P. J., Solomon, S. C., Smith, D. E., Zuber, M. T., Simons, M., Wieczorek, M. A., et al. (2002). Localized gravity/topography admittance and correlation spectra on Mars: Implications for regional and global evolution: Localized admittance on MARS. *Journal of Geophysical Research*, *107*(E12), 19–1–19–25. https://doi.org/10.1029/2002JE001854

McGovern, P. J., Solomon, S. C., Smith, D. E., Zuber, M. T., Simons, M., Wieczorek, M. A., et al. (2004). Correction to localized gravity/topography admittance and correlation spectra on mars: Implications for regional and global evolution. *Journal of Geophysical Research*, *109*(E7), E07007. https://doi.org/10.1029/2004JE002286

McKenzie, D., Barnett, D. N., & Yuan, D.-N. (2002). The relationship between Martian gravity and topography. *Earth and Planetary Science Letters*, *195*(1–2), 1–16. https://doi.org/10.1016/S0012-821X(01)00555-6

Murphy, J. P., & King, S. D. (2024). Reconciling mars insight results, geoid, and melt evolution with 3d spherical models of convection. *Journal of Geophysical Research: Planets*, *129*(5), e2023JE008143. https://doi.org/10.1029/2023JE008143

Nerozzi, S. (2021). Supplementary data for "the north polar basal unit of mars: An amazonian record of surface processes and climate events" (Tech. Rep. No. Version 1) [Dataset]. *University of Arizona Research Data Repository*. https://doi.org/10.25422/azu.data.12814340.v1

Nerozzi, S., Ortiz, M. R., & Holt, J. W. (2022). The north polar basal unit of mars: An amazonian record of surface processes and climate events. *Icarus*, *373*, 114716. https://doi.org/10.1016/j.icarus.2021.114716

Neukum, G., Jaumann, R., Hoffmann, H., Hauber, E., Head, J. W., Basilevsky, A. T., et al. (2004). Recent and episodic volcanic and glacial activity on mars revealed by the high resolution stereo camera. *Nature*, *432*(7020), 971–979. https://doi.org/10.1038/nature03231

Neumann, G. A., Rowlands, D. D., Lemoine, F. G., Smith, D. E., & Zuber, M. T. (2001). Crossover analysis of Mars Orbiter Laser Altimeter data. *Journal of Geophysical Research*, *106*(E10), 23753–23768. https://doi.org/10.1029/2000JE001381

Neumann, G. A., Zuber, M. T., Wieczorek, M. A., McGovern, P. J., Lemoine, F. G., & Smith, D. E. (2004). Crustal structure of Mars from gravity and topography. *Journal of Geophysical Research*, *109*(E8), E08002. https://doi.org/10.1029/2004JE002262

Novák, P., & Grafarend, E. W. (2006). The effect of topographical and atmospheric masses on spaceborne gravimetric and gradiometric data. *Studia Geophysica et Geodaetica*, *50*(4), 549–582. https://doi.org/10.1007/s11200-006-0035-7

Nyquist, L. E., Bogard, D. D., Shih, C. Y., Greshake, A., Stöffler, D., & Eugster, O. (2001). Ages and geologic histories of martian meteorites. *Space Science Reviews*, *96*(1), 105–164. https://doi.org/10.1023/A:1011993105172

Özeren, M., Sengor, A. M. C., Acar, D., & Älgen, S. C. (2014). *Valles marineris as a cryokarstic structure formed by a giant dyke system support from new analogue experiments* (pp. 1–2). AGU.

Phillips, R. J., Zuber, M. T., Smrekar, S. E., Mellon, M. T., Head, J. W., Tanaka, K. L., et al. (2008). Mars north polar deposits: Stratigraphy, age, and geodynamical response. *Science*, *320*(5880), 1182–1185. https://doi.org/10.1126/science.1157546

Phillips, R. J., Zuber, M. T., Solomon, S. C., Golombek, M. P., Jakosky, B. M., Banerdt, W. B., et al. (2001). Ancient geodynamics and global-scale hydrology on Mars. *Science*, *291*(5513), 2587–2591. https://doi.org/10.1126/science.1058701

Plesa, A.-C., Grott, M., Tosi, N., Breuer, D., Spohn, T., & Wieczorek, M. A. (2016). How large are present-day heat flux variations across the surface of mars? *Journal of Geophysical Research: Planets*, *121*(12), 2386–2403. https://doi.org/10.1002/2016JE005126

Plesa, A.-C., Knapmeyer, M., Golombek, M. P., Breuer, D., Grott, M., Kawamura, T., et al. (2018). Present-Day mars' seismicity predicted from 3-D thermal evolution models of interior dynamics. *Geophysical Research Letters*, *45*(6), 2580–2589. https://doi.org/10.1002/2017GL076124

Ratcliff, J. T., Bercovici, D., Schubert, G., & Kroenke, L. W. (1998). Mantle plume heads and the initiation of plate tectonic reorganizations. *Earth and Planetary Science Letters*, *156*(3), 195–207. https://doi.org/10.1016/S0012-821X(98)00016-8

Redmond, H. L., & King, S. D. (2004). A numerical study of a mantle plume beneath the Tharsis Rise: Reconciling dynamic uplift and lithospheric support models. *Journal of Geophysical Research*, *109*(E09008), 14. https://doi.org/10.1029/2003JE002228

Reusen, J. M., Root, B. C., Szwillus, W., Fullea, J., & van der Wal, W. (2020). Long-wavelength gravity field constraint on the lower mantle viscosity in North America. *Journal of Geophysical Research: Solid Earth*, *125*(12), e2020JB020484. https://doi.org/10.1029/2020JB020484

Roberts, J. H., & Zhong, S. (2007). The cause for the north-south orientation of the crustal dichotomy and the equatorial location of tharsis on mars. *Icarus*, *190*(1), 24–31. https://doi.org/10.1016/j.icarus.2007.03.002

Root, B. (2021). GSH is a matlab package to do global spherical harmonic analyses (GSHA) and synthesis (GSHS) for CRUST1.0. 4TU [Dataset]. *ResearchData*. https://doi.org/10.4121/16764238.v1

Root, B., Novák, P., Dirkx, D., Kaban, M., van der Wal, W., & Vermeersen, L. (2016). On a spectral method for forward gravity field modelling. *Journal of Geodynamics*, *97*, 22–30. https://doi.org/10.1016/j.jog.2016.02.008

Samuel, H., Ballmer, M. D., Padovan, S., Tosi, N., Rivoldini, A., & Plesa, A.-C. (2021). The thermo-chemical evolution of mars with a strongly stratified mantle. *Journal of Geophysical Research: Planets*, *126*(4), e2020JE006613. https://doi.org/10.1029/2020JE006613

Schubert, G., Bercovici, D., & Glatzmaier, G. A. (1990). Mantle dynamics in mars and venus: Influence of an immobile lithosphere on three-dimensional mantle convection. *Journal of Geophysical Research*, *95*(B9), 14105–14129. https://doi.org/10.1029/JB095iB09p14105

Schumacher, S., & Breuer, D. (2006). Influence of a variable thermal conductivity on the thermochemical evolution of mars. *Journal of Geophysical Research*, *111*(E2), E02006. https://doi.org/10.1029/2005JE002429

Searls, M. L., Banerdt, W. B., & Phillips, R. J. (2006). Utopia and hellas basins, mars: Twins separated at birth. *Journal of Geophysical Research*, *111*(E8), E08005. https://doi.org/10.1029/2005JE002666

Simons, M., Solomon, S. C., & Hager, B. H. (1997). Localization of gravity and topography: Constraints on the tectonics and mantle dynamics of Venus. *Geophysical Journal International*, *131*(1), 24–44. https://doi.org/10.1111/j.1365-246X.1997.tb00593.x

Smith, D., Lerch, F., Nerem, R., Zuber, M., Patel, G., Fricke, S., & Lemoine, F. (1993). An improved gravity model for mars: Goddard mars model 1. *Journal of Geophysical Research*, *98*(E11), 20871–20889. https://doi.org/10.1029/93je01839

Smith, D., Neumann, G., Arvidson, R. E., Guinness, E. A., & Slavney, S. (2003). *Mars global surveyor laser altimeter mission experiment gridded data record* (Tech. Rep. No. MGS-M-MOLA-5-MEGDR-L3-V1.0). NASA PLanetary Data System. https://doi.org/10.17189/1519460

Smith, D., Zuber, M., Neumann, G., & Slavney, S. (2003). Mars global surveyor laser altimeter mission experiment gridded data record [Dataset]. In *MGS-m-MOLA-5-MEGDR-l3-v1.0. NASA planetary data System*. Dataset used for Mars topography analysis, Creative Commons Zero v1.0 Universal. https://doi.org/10.17189/1519460

Smith, D., Zuber, M. T., Frey, H. V., Garvin, J. B., Head, J. W., Muhleman, D. O., et al. (2001). Mars Orbiter Laser Altimeter: Experiment summary after the first year of global mapping of Mars. *Journal of Geophysical Research*, *106*(E10), 23689–23722. https://doi.org/10.1029/2000JE001364

Smrekar, S. E., Lognonné, P., Spohn, T., Banerdt, W. B., Breuer, D., Christensen, U., et al. (2019). Pre-mission InSights on the interior of Mars. *Space Science Reviews*, *215*(1), 1–72. https://doi.org/10.1007/s11214-018-0563-9

Stähler, S. C., Khan, A., Banerdt, W. B., Lognonné, P., Giardini, D., Ceylan, S., & Smrekar, S. E. (2021). Seismic detection of the martian core. *Science*, *373*(6553), 443–448. https://doi.org/10.1126/science.abi7730

Steinberger, B., & Antretter, M. (2006). Conduit diameter and buoyant rising speed of mantle plumes: Implications for the motion of hot spots and shape of plume conduits. *Geochemistry, Geophysics, Geosystems*, *7*(11), Q11018. https://doi.org/10.1029/2006GC001409

Steinberger, B., Werner, S. C., & Torsvik, T. H. (2010). Deep versus shallow origin of gravity anomalies, topography and volcanism on Earth, Venus and Mars. *Icarus*, *207*(2), 564–577. https://doi.org/10.1016/j.icarus.2009.12.025

Taylor, N. C., Johnson, J. H., Herd, R. A., & Regan, C. E. (2020). What can Olympus mons tell us about the Martian lithosphere? *Journal of Volcanology and Geothermal Research*, *402*, 106981. https://doi.org/10.1016/j.jvolgeores.2020.106981

Thieulot, C., Blasweiler, M., & Root, B. (2023). The changing gravity field due to a superplume under the tharsis region. In *The changing gravity field due to a superplume under the tharsis region* (p. 1). Copernicus Meetings. Retrieved 2020-11-19, from Retrieved from http://posters.geo.uu.nl/2023/The_changing_gravity_field_due_to_a_superplume_under_the_Tharsis_Region-Thieulot_Blasweiler_Root-April2023.pdf

Torsvik, T. H., Steinberger, B., Cocks, L. R. M., & Burke, K. (2008). Longitude: Linking earth's ancient surface to its deep interior. *Earth and Planetary Science Letters*, *276*(3), 273–282. https://doi.org/10.1016/j.epsl.2008.09.026

Tosi, N. (2008). *Numerical modeling of present-day mantle convection*. Unpublished doctoral dissertation. Charles University, Faculty of Mathematics and Physics. Retrieved from https://geo.mff.cuni.cz/theses/2008-Tosi-PhD.pdf

Tosi, N., Martinec, Z., & Root, B. (2024). Modified spectral finite element code (SFEC). 4TU [Dataset]. *ResearchData*. https://doi.org/10.4121/0117f7c1-2ccc-4249-bde7-5f1607955a4f.v1

Turcotte, D. L., Willemann, R. J., Haxby, W. F., & Norberry, J. (1981). Role of membrane stresses in the support of planetary topography. *Journal of Geophysical Research*, *86*(B5), 3951–3959. https://doi.org/10.1029/JB086iB05p03951

Wagner, N. L., & James, P. B. (2025). New geophysical constraints for intrusive magmatism at large martian volcanoes: Implications for crustal thickness and volatile outgassing. *Journal of Geophysical Research: Planets*, *130*(8), e2025JE008959. https://doi.org/10.1029/2025JE008959

Wagner, N. L., James, P. B., Ermakov, A. I., & Sori, M. M. (2024). Evaluating the use of seasonal surface displacements and time-variable gravity to constrain the interior of mars. *Journal of Geophysical Research: Planets*, *129*(6), e2023JE008053. https://doi.org/10.1029/2023JE008053

Watts, A. (2001). *Isostasy and flexure of the lithosphere*. Cambridge University Press.

Wieczorek, M. A., Broquet, A., McLennan, S. M., Rivoldini, A., Golombek, M., Antonangeli, D., et al. (2022). Insight constraints on the global character of the martian crust. *Journal of Geophysical Research: Planets*, *127*(5), e2022JE007298. https://doi.org/10.1029/2022JE007298

Wieczorek, M. A., & Zuber, M. T. (2004). Thickness of the Martian crust: Improved constraints from geoid-to-topography ratios. *Journal of Geophysical Research*, *109*(E1), E01009. https://doi.org/10.1029/2003JE002153

Wörner, L., Root, B., Bouyer, P., Braxmaier, C., Dirkx, D., Encarnacao, J., & Witasse, O. (2023). Maquis - Concept for a mars quantum gravity mission. *Planetary and Space Science*, *239*, 105800. https://doi.org/10.1016/j.pss.2023.105800

Zhao, G., Liu, J., Chen, B., Kaban, M. K., & Du, J. (2021). 3-d density structure of the lunar mascon basins revealed by a high-efficient gravity inversion of the grail data. *Journal of Geophysical Research: Planets*, *126*(5), e2021JE006841. https://doi.org/10.1029/2021JE006841

Zhong, S. (2009). Migration of tharsis volcanism on mars caused by differential rotation of the lithosphere. *Nature Geoscience*, *2*(1), 19–23. https://doi.org/10.1038/ngeo392

Zhong, S., & hong, S. (2002). Effects of lithosphere on the long-wavelength gravity anomalies and their implications for the formation of the Tharsis rise on Mars. *Journal of Geophysical Research*, *107*(E7), 5054. https://doi.org/10.1029/2001JE001589

Zhong, S., & Roberts, J. H. (2003). On the support of the tharsis rise on mars. *Earth and Planetary Science Letters*, *214*(1), 1–9. https://doi.org/10.1016/S0012-821X(03)00384-4

Zuber, M. T., Lemoine, F. G., Smith, D. E., Konopliv, A. S., Smrekar, S. E., & Asmar, S. W. (2007). Mars reconnaissance orbiter radio science gravity investigation. *Journal of Geophysical Research*, *112*(E5), E05S07. https://doi.org/10.1029/2006JE002833

Zuber, M. T., Solomon, S. C., Phillips, R. J., Smith, D. E., Tyler, G. L., Aharonson, O., et al. (2000). Internal structure and early thermal evolution of Mars from Mars global surveyor topography and gravity. *Science*, *287*(5459), 1788–1793. https://doi.org/10.1126/science.287.5459.1788